Structure and Statistical Analysis of the Microphysical Properties of Generating Cells in the Comma Head Region of Continental Winter Cyclones

DAVID M. PLUMMER, GREG M. MCFARQUHAR, ROBERT M. RAUBER, AND BRIAN F. JEWETT

Department of Atmospheric Sciences, University of Illinois at Urbana–Champaign, Urbana, Illinois

DAVID C. LEON

Department of Atmospheric Science, University of Wyoming, Laramie, Wyoming

(Manuscript received 10 April 2014, in final form 1 July 2014)

ABSTRACT

This paper presents analyses of the microphysical structure of cloud-top convective generating cells at temperatures between −10° and −55°C across the comma head of 11 continental cyclones, using data collected by the W-band Wyoming Cloud Radar and in situ instrumentation aboard the National Science Foundation (NSF)/NCAR C-130. A case study of one cyclone is presented, followed by statistical analyses of the entire dataset.

Ice particle number concentrations averaged 1.9 times larger inside generating cells compared to outside, and derived ice water contents and median mass diameters averaged 2.2 and 1.1 times larger in cells, respectively. Supercooled water was directly measured at temperatures between −31.4° and −11.1°C, with the median and 95th-percentile liquid water content increasing from ~0.09 to 0.12 g m^{-3} and 0.14 to 0.28 g m^{-3} over this temperature range, respectively. Liquid water was present in 26% of observations within cells and 18% of observations between cells over the same temperature range, and it was nearly ubiquitous at temperatures above −16°C.

The larger ice particle concentrations in cells are consistent with greater ice production in convective updrafts. The increased mass and diameter of the ice particles demonstrate that generating cells provide environments favorable for enhanced particle growth. The impact of water saturation and supercooled water in the cells was evident, with rapid particle growth by diffusion and sometimes riming apparent, in addition to aggregation. Turbulent mixing lessened the observed differences between cells and surrounding regions, with supercooled water observed within and between cells, similar habits within and between cells, and rimed particles evident even in ice-phase conditions.

1. Introduction

The comma head of cold-season extratropical cyclones is often characterized by embedded substructures, such as linear precipitation bands and cloud-top convective generating cells (GCs).[1] Early studies using vertically pointing radars, such as those of Marshall (1953), Gunn et al. (1954), Boucher (1959), Wexler (1955), Langleben (1956), Douglas et al. (1957), and Wexler and Atlas (1959), noted kilometer-scale GC activity near cloud top that produced precipitation streamers, or fall streaks, into stratiform cloud layers below. Subsequent research involving Doppler radar (Carbone and Bohne 1975) estimated maximum vertical velocities on the order of ±1.5 m s^{-1} for the GC convection. More recently, Rosenow et al. (2014) reported statistical analyses of GC vertical motions using cloud radar measurements obtained across the comma head of three continental cyclones, finding that the GCs were typically 1–2 km deep, had horizontal scales of ~0.5–2 km, and had vertical velocities of ±1–2 m s^{-1}.

Many studies (e.g., Houze et al. 1981; Browning 1983; Rutledge and Hobbs 1983; Bader et al. 1987; Sienkiewicz et al. 1989; Syrett et al. 1995; Trapp et al. 2001; Schultz et al. 2004; Stark et al. 2013; Cunningham and Yuter 2014)

[1] The term "generating cell" describes a small region of locally high radar reflectivity at cloud top from which an enhanced reflectivity trail characteristic of falling snow particles originates (American Meteorological Society 2013).

Corresponding author address: David M. Plummer, Department of Atmospheric Sciences, University of Illinois at Urbana–Champaign, 105 S. Gregory Street, Urbana, Illinois 61801.
E-mail: dplumme2@illinois.edu

DOI: 10.1175/JAS-D-14-0100.1

have investigated GCs as components of a "seeder–feeder" mechanism (Bergeron 1950). The GCs act to "seed" ice particles into a stratiform "feeder" layer below, in which large-scale convergence provides an enhanced moisture source for particle growth below the GC level (Herzegh and Hobbs 1980; Matejka et al. 1980; Browning 1983; Rutledge and Hobbs 1983).

While most studies of GCs have used remote sensing and surface-based observations, few studies have reported measurements within GCs themselves to understand the microphysical processes occurring within them. In situ measurements in GCs within one cyclone at temperatures near −14°C showed the presence of supercooled liquid water (SLW) and 2–3-times enhanced ice particle concentrations within the GCs compared to surrounding regions, allowing Houze et al. (1981) to hypothesize that enhanced nucleation and initial particle growth were occurring in the GCs. Along with prior work (Houze et al. 1976; Matejka et al. 1980; Herzegh and Hobbs 1980), they determined that ~80% of particle growth occurred below the GC level, with depositional growth occurring within the cells, and both deposition and (at temperatures approaching 0°C) aggregation being important in the stratiform layer below. More recently, Wolde and Vali (2002) analyzed data from spiral descents within and below GCs for two cases with GCs directly sampled near −29°C. Although most of their measurements took place below the GC level, they observed enhanced ice concentrations as well as low SLW contents (LWCs) of ~0.03 g m^{-3} in measurements near cloud top. Evans et al. (2005) also identified GCs near both −20°C and −45° to −50°C in one cyclone in the Pacific Northwest. Their measurements indicated enhanced concentrations of cloud droplets within the GCs near −20°C, but not of larger ice particles. They concluded that the GCs were sampled early enough in their life cycle that they had not produced many larger ice particles. They also concluded that depositional growth was dominant within GCs and associated fall streaks, with aggregation becoming more important at higher temperatures. Ikeda et al. (2007) described measurements within two cyclones, sampling GCs directly near −20° and −15°C. Ice particle concentrations were enhanced by a factor of 3–4 or more within the cells, and SLW was also encountered, with the largest LWCs near −15°C. Finally, Crosier et al. (2014) sampled cloud-top GCs below −40°C, consistently identifying enhanced ice water content (IWC) and particle number concentrations (up to an order of magnitude larger than in surrounding cloud) within the GCs.

While prior studies, combined, include measurements covering a large range of temperatures, the number of direct measurements within GCs in each case was typically quite limited. In this paper, the microphysical characteristics of GCs are analyzed using airborne cloud radar and in situ measurements obtained within 11 cold-season continental cyclones at temperatures between −10° and −55°C and in both ice- and mixed-phase environments. These data, obtained during the 2009–10 Profiling of Winter Storms (PLOWS) project (Rauber et al. 2014), considerably extend the previous studies in that 1) many more measurements covering various stages in the storms' life cycles were obtained, and 2) the in situ data were obtained with minimal bias due to shattering of ice crystals on the instrumentation and were coincident with high-resolution radar data to provide the appropriate context. Using a detailed case study of one cyclone and statistical analyses of the full dataset, the analyses quantitatively compare the size, shape, and phase distributions of cloud particles inside and outside of the generating cells, providing unique insight into the physical processes that determine the properties of the generating cells.

2. Data and methodology

The data used here were acquired during PLOWS with instrumentation aboard the National Science Foundation (NSF)/National Center for Atmospheric Research (NCAR) C-130 research aircraft, including the University of Wyoming Cloud Radar and Lidar (WCR; WCL; Wang et al. 2012) and a suite of in situ microphysical probes. The flight strategy used during PLOWS varied between cases. Most flights featured a combination of lengthy horizontal passes and shorter vertically stacked passes at several altitudes across cyclone comma head regions. Several flights (including the 15 February 2010 flight analyzed in section 3) consisted of vertical profiles made up of repeated passes between two waypoints at a larger number of altitudes.

A three-beam configuration was used for the WCR during PLOWS, with two vertical beams (upward and downward from the C-130) and one slanted beam (34.3° aft of nadir). Measurements of equivalent radar reflectivity factor Z_e and the vertical component of radial velocity W from the two vertical beams are used here, with data sampled at a range resolution of 15 m and a horizontal resolution corresponding to ~4–7.5 m at typical C-130 airspeeds during PLOWS. The WCR data were processed as described in Rosenow et al. (2014), following the same convention of using positive W values to indicate upward vertical motion. Furthermore, two additional processing techniques were applied. First, Z_e and W were estimated at the aircraft's location in order to compare against the in situ observations. Because the WCR did not record data within 105 m of the C-130, the data from the closest three pulse volumes above and below

the C-130 were interpolated to the aircraft's location, following Grim et al. (2007). Second, an objective radar-based estimate of cloud-top altitude was derived using threshold values for Z_e and σ_W^2, the variance of W. The σ_W^2 was calculated for each W measurement relative to the surrounding eight measurements using a noise threshold value of $\sigma_W^2 = 0.8\,\mathrm{m^2\,s^{-2}}$, following Rosenow et al. (2014). If a pulse volume with $\sigma_W^2 < 0.8\,\mathrm{m^2\,s^{-2}}$ for 12 consecutive vertical levels (180 m) and $Z_e > -25\,\mathrm{dBZ}_e$ occurred immediately below a measurement with $\sigma_W^2 > 0.8\,\mathrm{m^2\,s^{-2}}$ and $Z_e < -25\,\mathrm{dBZ}_e$, that measurement was classified as cloud top. Both criteria needed to be met to classify a pulse volume as being at cloud top, with the W variance threshold providing the primary indication of noisy echoes and the Z_e threshold generally correlating well with this as a supplementary noise check.

The air temperature T, presence and amount of SLW, and size and shape distributions of cloud and precipitation particles were obtained by probes installed on the C-130. The presence of SLW was identified using a Rosemount Icing Detector (RICE), which indicates SLW's presence using an output voltage change and is responsive to LWC $> 0.01\,\mathrm{g\,m^{-3}}$ (Cober et al. 2001). Measurements of LWC were obtained using a Commonwealth Scientific and Industrial Research Organisation (CSIRO) King probe and a Gerber particle volume monitor (PVM). The number distribution functions for small particles were measured by a cloud droplet probe (CDP) for particles with maximum dimensions D between 2 and 52 μm, and by two forward-scattering spectrometer probes (FSSPs), model 100, for $3 < D < 43\,\mu$m and $4 < D < 56\,\mu$m, the latter of which featured a modified inlet to reduce particle shattering. Because the shattering of large ice crystals on the tips and inlets of forward-scattering probes can generate artificially high numbers of small ice crystals, the FSSP data are only used for liquid- or mixed-phase clouds (e.g., Gardiner and Hallett 1985; McFarquhar and Cober 2004; McFarquhar et al. 2007a).

The size and shape distributions of larger particles were measured using two-dimensional cloud and precipitation optical array probes (2D-C and 2D-P) with nominal size ranges of 25–1600 μm (2D-C) and 200–6400 μm (2D-P). The 2D-C and 2D-P measurements were processed using software developed in-house, with reconstruction techniques used to calculate D for particles partially outside of the field of view (e.g., Heymsfield and Parrish 1978). Measurements from the 2D-C were used for particles with $500 \le D \le 2000\,\mu$m, with measurements from the 2D-P used for larger particles. The lower size threshold for the 2D-C was chosen to eliminate poorly defined sample volumes for particles with $D < \sim 150\,\mu$m (Baumgardner and Korolev 1997) and to minimize the effect of particle shattering, which primarily affects particles with $D < 500\,\mu$m (Korolev et al. 2013; Jackson et al. 2014). The crossover between the 2D-C and 2D-P at 2000 μm was larger than the $\sim$1000 μm value typically used (Jackson et al. 2012), to account for additional processing techniques correcting reduced sensitivity in a portion of the 2D-P photodiode array (detailed in the appendix).

Thereafter, number concentrations $N_{>500}$ and number distribution functions $N(D)$ were derived from the composite 2D-C and 2D-P measurements. Ice water content and mass distribution functions $m(D)$ were estimated using the projected area of each particle, following Baker and Lawson (2006).[2] The IWC estimates were also used to calculate the median particle dimension with respect to mass D_{mm} for the combined 2D-C and 2D-P size distributions. Note that the derived IWC and D_{mm} values only include particles with $D > 500\,\mu$m, unless specified otherwise, because of the measurements uncertainties described above. Because of the finescale nature of the convective features, measurements were generally averaged over 5-s periods in this study, although a range of averaging times was also tested (see section 4). Additionally, an automated phase identification algorithm incorporating King, RICE, FSSP, and 2D-C measurements (McFarquhar et al. 2007b; Jackson et al. 2012) was also used to classify the in situ measurements based on their phase characteristics (ice, liquid, or mixed-phase).

3. 14–15 February 2010 case study

For convenience, the term "GC regions" is used here to refer to the general areas where GCs were present at cloud top, as indicated by cellular Z_e and convective W radar signatures. To illustrate the role of specific small-scale processes acting inside and outside generating cells, measurements acquired during the 15 February 2010 research flight are described first before the statistical properties of GCs are characterized using the entire PLOWS dataset. As described by Rosenow et al. (2014), the 14–15 February 2010 cyclone was an Alberta clipper–type system. Deep clouds within the cyclone's comma head and shallower clouds further to the southwest were sampled by the C-130 as the low-pressure center passed south of the operations area in southern

[2] A counterflow virtual impactor was employed during PLOWS to provide direct measurements of total mass content; however, instrumentation issues degraded the data quality enough to be unusable as a comparison to the 2D-derived mass estimates.

Indiana (Fig. 1). The C-130 performed two complete flight stacks of ~200 km in length over ~7 h at altitudes ranging from 2.6 to 7.4 km (all altitudes hereinafter refer to a value above mean sea level) and temperatures ranging from ~−11° to −52°C, as indicated in Figs. 1 and 2. A profile of the cyclone's structure in terms of WCR Z_e is shown in Fig. 2a for the flight leg from 0800 to 0819 UTC (approximately halfway through the mission), with lines showing the altitudes of the flight legs for the first (dashed) and second (dashed–dotted) set of stacked legs overlaid.

Representative features of the two general regions sampled within the cyclone are evident in Fig. 2a. The cyclone's deep comma head was present in the northeastern half of the profile and was composed of clouds and precipitation up to ~8-km altitude. A higher-resolution view of Z_e is shown to illustrate the GCs atop this region (Fig. 2b). Convective GCs with horizontal and vertical scales of 1–2 km were consistently observed at cloud top, with fall streaks emerging from the GCs and merging through the deeper cloud below. Rosenow et al. (2014) showed that vertical velocities of ± 1–$2\ \mathrm{m\ s^{-1}}$ were common in association with these GCs, with the strongest velocities confined to the GC level and weaker stratiform velocity signatures (close to the expected spectrum of particle terminal velocities) below the GC level. These signatures are apparent in Fig. 3a, which shows a W profile (uncorrected for particle fall velocities) along an earlier flight leg that illustrates the GCs occurring atop the deep comma head precipitation. Measurements from this leg are shown here because the aircraft was sampling below the GC region, where relatively weak vertical air motion at flight level did not degrade the W measurements. In contrast, Fig. 3b shows a W profile corresponding to a portion of the flight leg shown in Figs. 2a and 2b. For this segment, the aircraft was within the GC region. Visual confirmation of the turbulence in this region (and resulting inadequately resolved aircraft motion) is evident in the oscillations in vertical radial velocities even after correcting for horizontal wind contamination, seen as the high-frequency vertical "stripes" in Fig. 3b. Further southwest (prior to ~0810 UTC), an abrupt transition into shallower precipitation is evident in Fig. 2a, with radar echoes only present below ~3.5-km altitude. The precipitation in this region featured a similar structure to that in the deeper comma head, although at a much shallower scale: GCs were again evident at cloud top, producing fall streaks of hydrometeors that merged within the stratiform layer below. Figure 2c shows a Z_e profile for a flight segment when the aircraft was in the shallower GC region, and Fig. 3c shows W measurements within this region. Again, convective vertical motions are evident

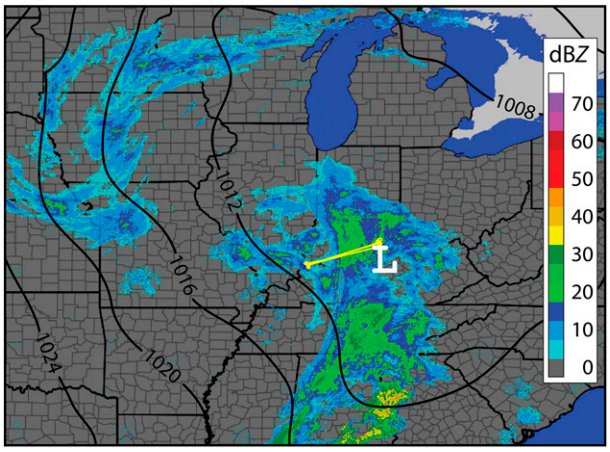

FIG. 1. WSR-88D composite reflectivity overlaid with Rapid Update Cycle mean sea level pressure analysis, both valid at 0800 UTC 15 February 2010, with the yellow line indicating the research flight track within the operations area over southern Indiana.

within the GC region, with turbulence at the aircraft level resulting in vertical stripes seen in the radial velocities from the downward-pointing vertical beam.

The structural characteristics shown in Figs. 2 and 3 were consistent over the course of the flight [see also section 3c in Rosenow et al. (2014)], with cloud-top GCs observed both above the deep comma head precipitation and the shallower clouds to the west. Air temperatures measured by the aircraft were between approximately −45° and −52°C in the GCs atop the deep comma head precipitation and between −17° and −26°C in the GCs at lower altitudes. Additionally, SLW was commonly observed within the generating cells atop the shallower clouds using backscattered power and depolarization measurements from the University of Wyoming Cloud Lidar onboard the C-130.

a. GC characteristics atop deep clouds

To better define the microphysical structure of GCs, Z_e measurements from the WCR and $N_{>500}$, IWC, and D_{mm} measured by the in situ instrumentation are shown in Fig. 4 for two representative flight legs that passed directly through GCs. The flight legs were chosen to include measurements made near GC tops and bases atop the deep comma head precipitation. When the aircraft was passing through GC regions (i.e., the convective Z_e and W signatures extended through flight level, as in Figs. 2b,c and 3b,c), 4-dB relative maxima in the Z_e time series measurements interpolated to the aircraft location were used to define the GC cores for the purposes of the statistical analyses described below. The analyses used 5-s averaging (representing ~500–750-m distance) to correspond to the range of GC widths of ~0.5–2 km determined by Rosenow et al. (2014).

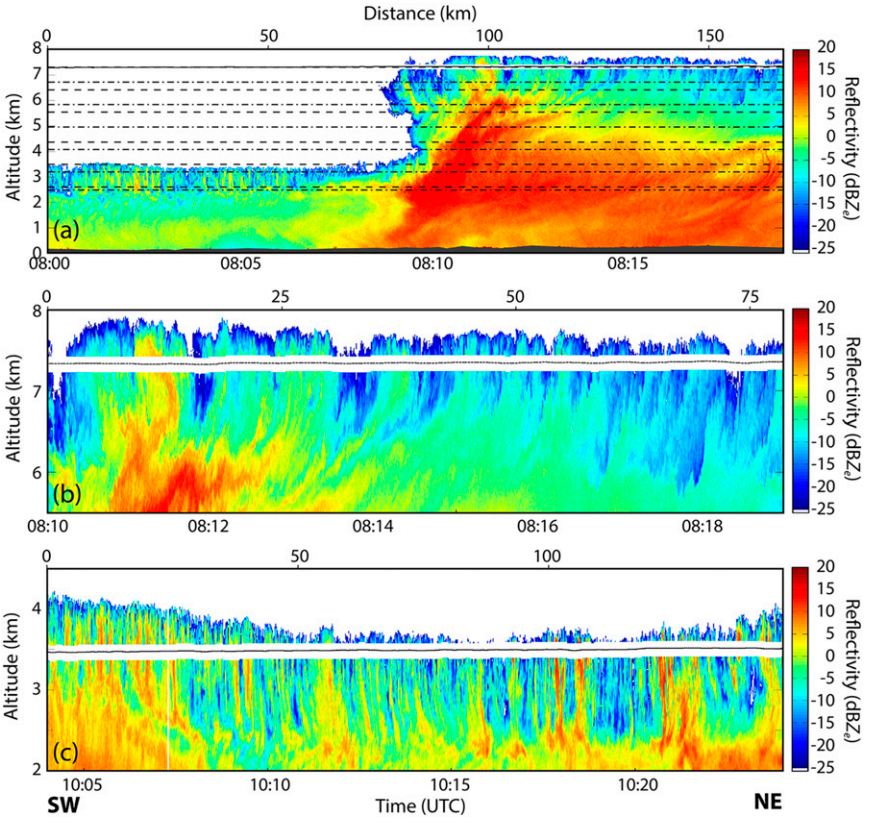

FIG. 2. (a) Z_e profile for the 0800–0819 UTC 15 February 2010 flight leg. Dashed lines indicate altitudes of aircraft passes along similar flight tracks between 0350 and 0720 UTC and dashed–dotted lines indicate passes between 0740 and 1100 UTC, (b) higher-resolution Z_e profile for 0810–0819 UTC, and (c) Z_e profile for 1004–1024 UTC, representative of the shallower precipitation region in the southwestern half of (a).

Statistics were then calculated separately for the 5-s measurements encompassing Z_e peaks and the measurements not containing them. Hereinafter, these regions are referred to as GC cores and regions between GC cores, respectively. While the proportion of each flight leg identified as GC cores depends on the classification criteria used, time periods corresponding to these criteria are shaded gray in Figs. 4a and 4c. The results of any analyses depend on the exact criteria used, but the trends described below are broadly consistent over various Z_e thresholds and averaging windows (described in section 4). To provide a larger sample size for the GCs atop deep clouds, the in situ statistics described below include measurements obtained during additional passes from the same flight at similar altitudes and temperatures to those shown in Fig. 4. The median and 5th, 25th, 75th, and 95th percentiles of $N_{>500}$, IWC, and D_{mm} as a function of altitude are shown with box-and-whisker plots in Fig. 5, and Fig. 6 shows averaged $N(D)$ for the same data. Each figure shows measurements separately within and between the GC cores.

For the higher-altitude GCs (e.g., the northeast portion of Fig. 2a), time series measurements from two flight legs are shown in Fig. 4. The shading around the in situ parameters indicates their fractional uncertainty based on $p^{0.5}$, where p is the total number of observed particles in each 5-s average. The 7.3-km-altitude flight leg (Figs. 4a,b; 0810–0819 UTC) is composed of measurements near GC tops at a mean air temperature $\overline{T}$ of $-51° \pm 0.3°$C. The additional measurements contributing to the in situ statistics are from 0737:50–0743:40 UTC, with the same average altitude and temperature, and the 6.8-km-altitude leg (Figs. 4c,d; 0439–0446:30 UTC) sampled near GC bases with $\overline{T} = -44° \pm 0.1°$C. The additional flight segments contributing to the statistics are from 0339:50–0343:10, 0357:00–0400:15, 0412:00–0416:20, and 0823:30–0830:00 UTC, with average altitude 6.7 km and average temperature −43.8°C overall. For these flight legs, Z_e was only briefly greater than 0 dBZ_e. The measurements were in ice-phase conditions, as evidenced from the temperatures of these flight legs and weak, noisy signals in the King, PVM, and RICE measurements (not

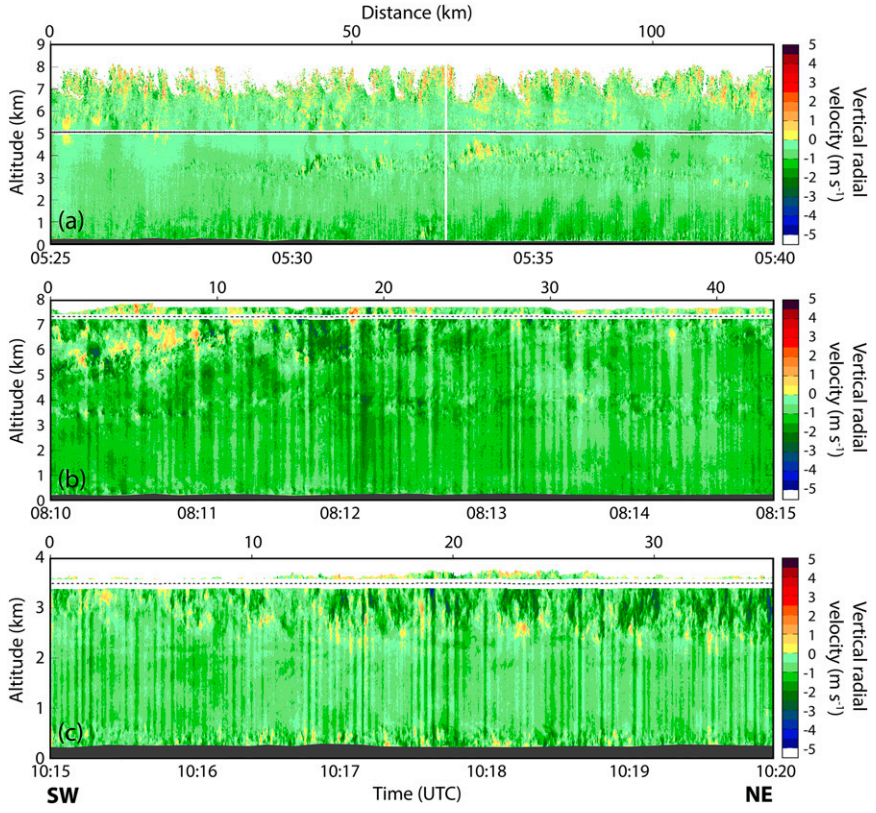

FIG. 3. Profiles of W during the 15 February 2010 research flight, valid for (a) 0525–0540, (b) 0810–0815, and (c) 1015–1020 UTC, with positive W values indicating upward vertical motion. The vertical stripes in (b) and (c) are caused by turbulence at the GC level rocking the aircraft so that the beams tilted and thus measured both vertical particle motion and a component of the horizontal wind.

shown). The $N_{>500}$ values (Figs. 4a,c) along both flight legs depicted are synchronized with the lower-frequency oscillations of Z_e. For the GC cores, the median $N_{>500}$ was 5.5 for the 7.3-km altitude measurements and 4.9 L^{-1} for the 6.7-km measurements, with the 5th and 95th percentiles spanning 1.5–12.1 and 0.5–11.3 L^{-1} (Fig. 5a). Between GC cores, $N_{>500}$ were consistently smaller. The median values were 2.8 and 2.2 L^{-1}, with the 5th–95th percentiles 0.4–8.2 and 0.1–6.3 L^{-1} for the 7.3- and 6.7-km measurements, respectively.

Larger IWC and D_{mm} were associated with the GCs compared to regions outside the GC cores (Figs. 4b,d). The median IWC within the cores was ~0.1 g m^{-3} for both flight legs (Fig. 5b). The IWCs only briefly surpassed 0.20 g m^{-3} in the GC cores, with the 5th–95th percentiles spanning 0.02–0.32 g m^{-3} for the 7.3-km measurements and 0.01–0.22 g m^{-3} for the 6.7-km measurements (Fig. 5b). The IWC percentiles were predominantly 2–3 times larger or more within the GC cores compared to between the GCs. The D_{mm} values showed similar trends in both cases. The median D_{mm} values in GC cores were 705 and 660 μm for the 7.3- and 6.7-km measurements, and the 5th–95th percentiles spanned ~580–970 and ~545–890 μm, respectively (Fig. 5c). The percentile D_{mm} values were ~10% larger on average within the GCs than outside. The averaged $N(D)$ for both legs (red and orange lines in Fig. 6) featured enhanced values for all D within the GC cores, and had generally similar slopes in both cases for measurements within (solid lines) and between the cores (dashed lines). The values were ~1.5–4 times larger within the cores over most of the size range.

Figure 7 shows 2D-C image records corresponding to the 7.3- and 6.8-km altitude flight legs in Fig. 4, with Figs. 7a and 7b composed of measurements within GC cores for the 7.3-km leg and Figs. 7c and 7d within cores for the 6.8-km leg. Figures 7e and 7f consist of measurements at Z_e minima between GC cores for the 7.3-km leg, and Figs. 7g and 7h do so for the 6.8-km leg. The 2D-C imagery indicated a mix of small irregular crystals and bullet rosettes, as well as some columns, consistent with ice growth by vapor deposition (e.g., Bailey and Hallett 2009). Additionally, similar habits were visually identifiable within and between the GCs for both flight legs, with

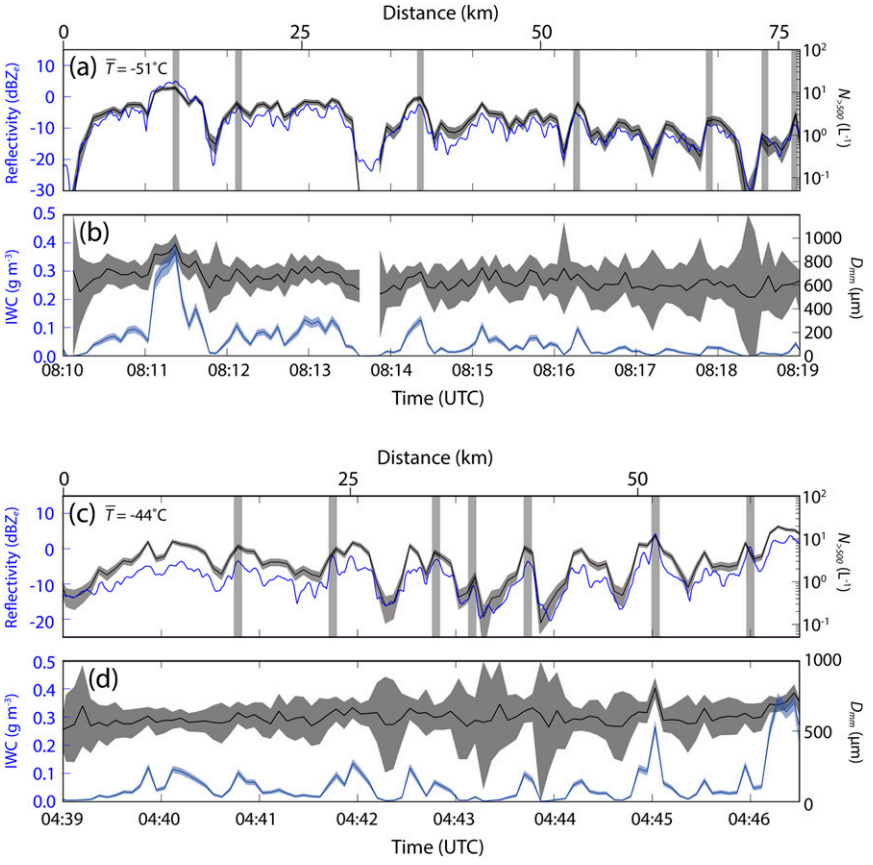

FIG. 4. Time series of (a) Z_e (blue, left axis) and $N_{>500}$ (black, right axis); (b) IWC (blue, left axis) and D_{mm} (black, right axis), for the 7.3-km-altitude flight leg, valid 0810–0819 UTC 15 February 2010. (c),(d) The same parameters for the 6.8-km-altitude flight leg, valid for 0439–0446:30 UTC 15 February 2010. Shading around the $N_{>500}$, IWC, and D_{mm} values indicates fractional uncertainty in measurements based on $p^{0.5}$. Vertical gray boxes in (a) and (c) indicate 5-s intervals classified as GC cores according to 4-dB relative maxima in Z_e after smoothing to address very finescale variability.

the most notable difference being the increased number of large particles within the GC cores compared to outside them. The signatures evident in $N_{>500}$, IWC, D_{mm}, and $N(D)$ along both flight legs are consistent with the GC convection acting to enhance ice nucleation as well as provide an environment favorable for particle growth via deposition within the GCs. The characteristics of the particles within and between the cells suggest that the turbulent nature of the region (supported by the velocity signatures seen in Fig. 3b) acts to reduce some of the differences between the cell cores and the surrounding regions; this is discussed further below.

b. GC characteristics atop shallow clouds

The time series measurements of Z_e and $N_{>500}$, LWC, RICE voltage, IWC, and D_{mm} for the GCs atop the shallower precipitation are shown in Fig. 8, with the statistical percentiles summarized in Fig. 5. The 3.5-km-altitude leg is composed of measurements near GC tops with $\overline{T} = -24° \pm 1.2°C$ (Figs. 8a–c; 1004–1024 UTC), and the 2.6-km leg of measurements near GC bases with $\overline{T} = -17° \pm 1.0°C$ (Figs. 8d–f; 1033–1048 UTC). Increased median and maximum Z_e values in GC cores were evident compared to the higher-altitude measurements. Whereas only a few measurements exceeded 0 dBZ_e along the higher legs, the median values were near or above 0 dBZ_e for both lower legs, with 95th percentiles 9–12 dBZ_e. The $N_{>500}$ measurements (Figs. 8a,d) were synchronized with the lower-frequency trends of Z_e, maximizing locally where Z_e increased in the cores. The median $N_{>500}$ within the GC cores (Fig. 5a) increased slightly from 2.4 L^{-1} for the 3.5-km altitude leg to 2.7 L^{-1} for the 2.6-km leg, and the 5th–95th-percentile range increased from 0.3–7.3 to 1.1–10.8 L^{-1} (Fig. 5a). This compared to median $N_{>500}$ values between the GCs of 1.4 and 1.6 L^{-1}, and 5th–95th percentiles of 0.2–5.3 and

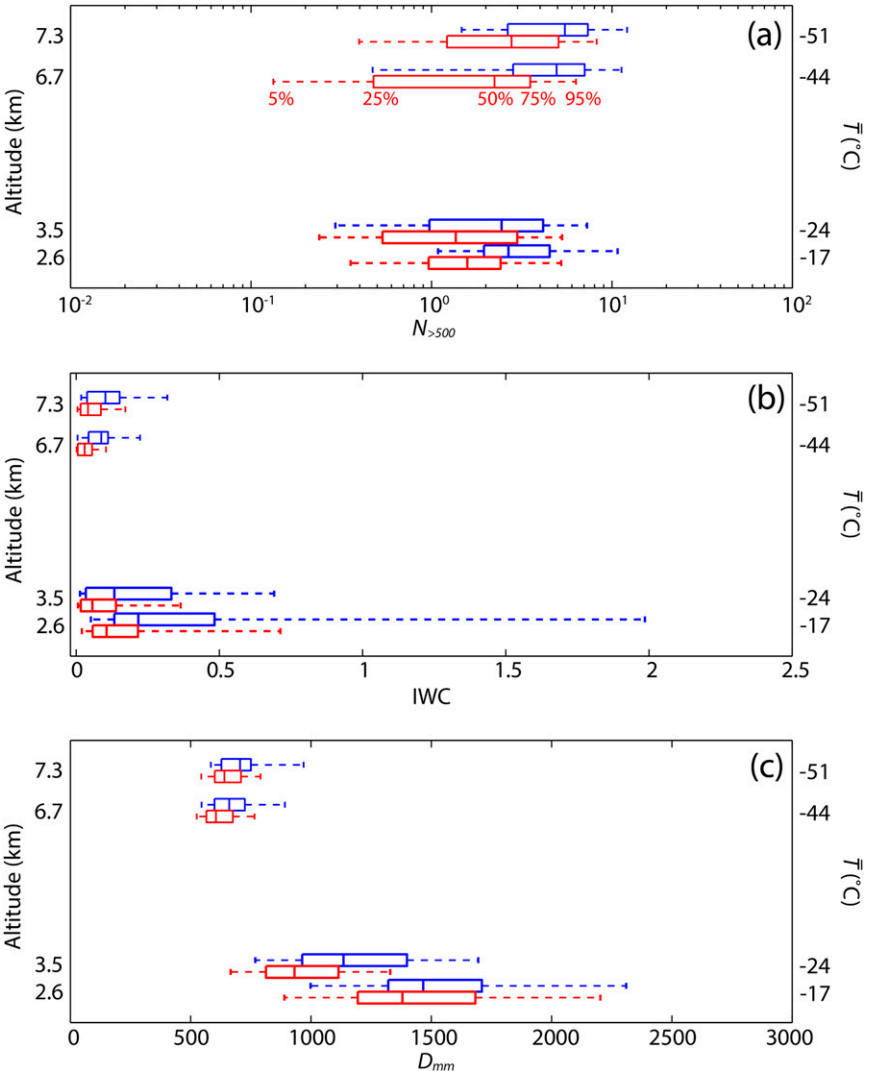

FIG. 5. Median and 5th, 25th, 75th, and 95th percentiles for (a) $N_{>500}$ (L^{-1}), (b) IWC ($g\,m^{-3}$), and (c) D_{mm} (μm) for flight legs at 7.3-, 6.8-, 3.5-, and 2.6-km altitude from the 15 February 2010 research flight. The median and percentiles in blue are for measurements within GC cores, and the median and percentiles in red are between GCs.

0.4–5.2 L^{-1} for the 3.5- and 2.6- legs. With the exception of some of the outer percentiles, the $N_{>500}$ statistics were generally smaller in each case, compared to the higher-altitude measurements.

The median IWCs within the GC cores were 0.13 and 0.22 $g\,m^{-3}$ for the 3.5- and 2.6-km legs, with the 95th-percentile values increasing to 0.69 and 1.99 $g\,m^{-3}$, respectively (Figs. 5b and 8b,d). Again, IWC percentile values within the GC cores were typically 2–3 times larger than between the GCs. The median D_{mm} values for the 3.5- and 2.6-km legs were ~1135 and 1470 μm within the GCs, with the 5th and 95th percentiles spanning ~770–1700 and 1000–2300 μm (Fig. 5c). The 95th-percentile D_{mm} values were ~10%–30% larger within the GC cores compared to between them. Both within and between the GCs, lower concentrations of small particles ($D <$ ~1000 μm) were evident in the averaged $N(D)$ at 3.5- and 2.6-km altitude (green and blue lines in Fig. 6) compared to the higher-altitude measurements, and measurements extended to larger particles for the lower-altitude legs. The $N(D)$ values were consistently enhanced by a factor of ~1.5–3 within the cells over much of the size range, with the enhancements greater for the 2.6-km leg. The ratio increased with D for both legs, particularly for $D >$ ~2000 μm. The larger particles evident in the 2.6-km leg near GC base, as compared to the 3.5-km leg, are suggestive of the effects of sedimentation as terminal velocities increase for larger ice particles.

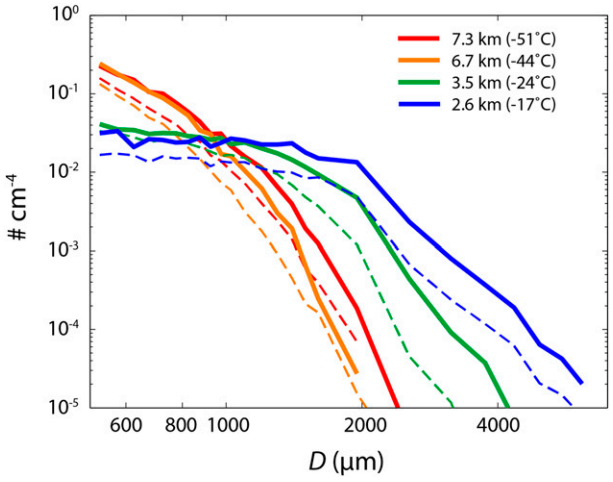

FIG. 6. Averaged $N(D)$ for four flight legs during the 15 February 2010 research flight, with coloring indicating the 0810–0819 (red), 0439–0446:30 (orange), 1004–1024 (green), and 1033–1048 UTC (blue) flight segments, respectively, for measurements within (solid) and between (dashed) GC cores.

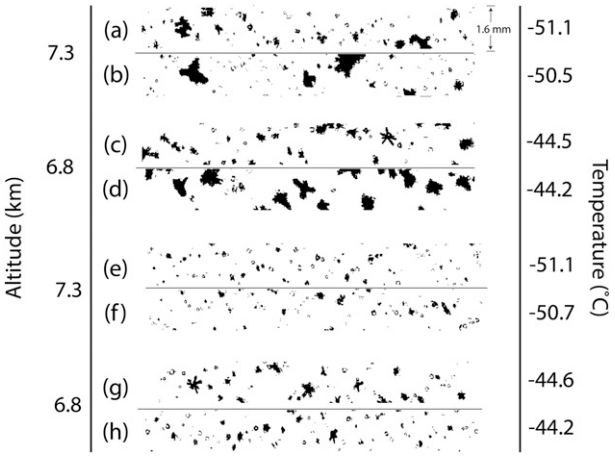

FIG. 7. Shown are 2D-C shadow images from GC regions sampled during the 15 February 2010 research flight, relative to altitude and air temperature, corresponding to the flight segments in Fig. 4. Image records valid for (a) 0814:23, (b) 0811:23, (c) 0425:03, (d) 0445:00, (e) 0814:35, (f) 0811:47, (g) 0425:03, and (h) 0444:40 UTC. (a)–(d) Measurements within GC cores and (e)–(h) measurements at Z_e minima between GCs.

A major difference between the higher- and lower-altitude flight legs was the presence of SLW at the lower altitudes. Liquid water has been measured at cloud top in a variety of environments in past studies [e.g., Rauber and Grant (1986) in orographic clouds; McFarquhar et al. (2011) in Arctic stratocumulus] and has major impacts on both ice nucleation and growth. Rauber and Tokay (1991) provide a theoretical basis for why SLW can exist in the cloud-top region. In the PLOWS dataset, the GCs occurring at higher temperatures atop shallow precipitation commonly had SLW present. In this cyclone, both flight legs at lower altitudes ($\overline{T} = -24°$ and $-17°$C) included segments in mixed-phase conditions, which occurred 55% of the time for the 3.5-km leg and 17% of the time for the 2.6-km leg. The King, PVM, and RICE measurements all indicated the presence of SLW near 1005 UTC and from approximately 1012 to 1022 and from 1033 to 1038 UTC (Figs. 8c,f). Visual inspection of 2D particle images also confirmed the presence of ice whenever SLW was present.

For time periods with LWC greater than a threshold of 0.05 g m^{-3}, median (95th percentiles) values of 0.14 (0.22) g m^{-3} and 0.17 (0.27) g m^{-3} were measured by the King probe and PVM, respectively, along the 3.5-km leg, compared to smaller values of 0.06 (0.12) g m^{-3} (King) and 0.07 (0.13) g m^{-3} (PVM) for the 2.6-km leg. Although the two flight legs on the 15 February 2010 flight would not have sampled the same GCs, as the cells evolve over time, the altitude and depth of the GCs were relatively consistent between the two legs. Thus, the larger LWCs measured near the GC tops are consistent with additional time for cooling as air ascends in convective updrafts. Based on calculations for parcel ascent using the conditions measured at 2.6-km altitude, the LWC values measured near cell tops were subadiabatic, suggesting that mixing/entrainment and ice particle growth acted to decrease the amount of SLW produced in the updrafts.

Figure 9 shows time series measurements of Z_e (black line) and LWC (blue and red lines) for a subsection of the 3.5-km-altitude leg from 1015 to 1018 UTC to identify the location of SLW relative to the position of the GC cores. It is seen that SLW was not exclusively encountered within GC cores, with LWC > 0.05 g m^{-3} commonly encountered between the GCs. This, combined with the inhomogeneities and small-scale structure, suggests that turbulence inherent to the GC regions acted to mix the SLW throughout the regions in the manner previously shown by Field et al. (2004) and McFarquhar et al. (2011) in other meteorological situations. Nevertheless, LWC percentiles were an average of 0.04 g m^{-3} larger within the GC cores for the 3.5-km and 2.6-km flight legs. These characteristics were typical of those encountered during other PLOWS research flights sampling GCs, which will be described in more detail in section 4.

The presence of supercooled water helps to explain the ice growth characteristics evident in the lower-altitude flight legs. Example 2D-C image records are shown in Fig. 10, with Figs. 10a–c comprised of measurements within GC cores along the 3.5-km leg and Figs. 10d–f along the 2.6 km leg. Figures 10g–i shows measurements between the GC cores for the 3.5 -km leg,

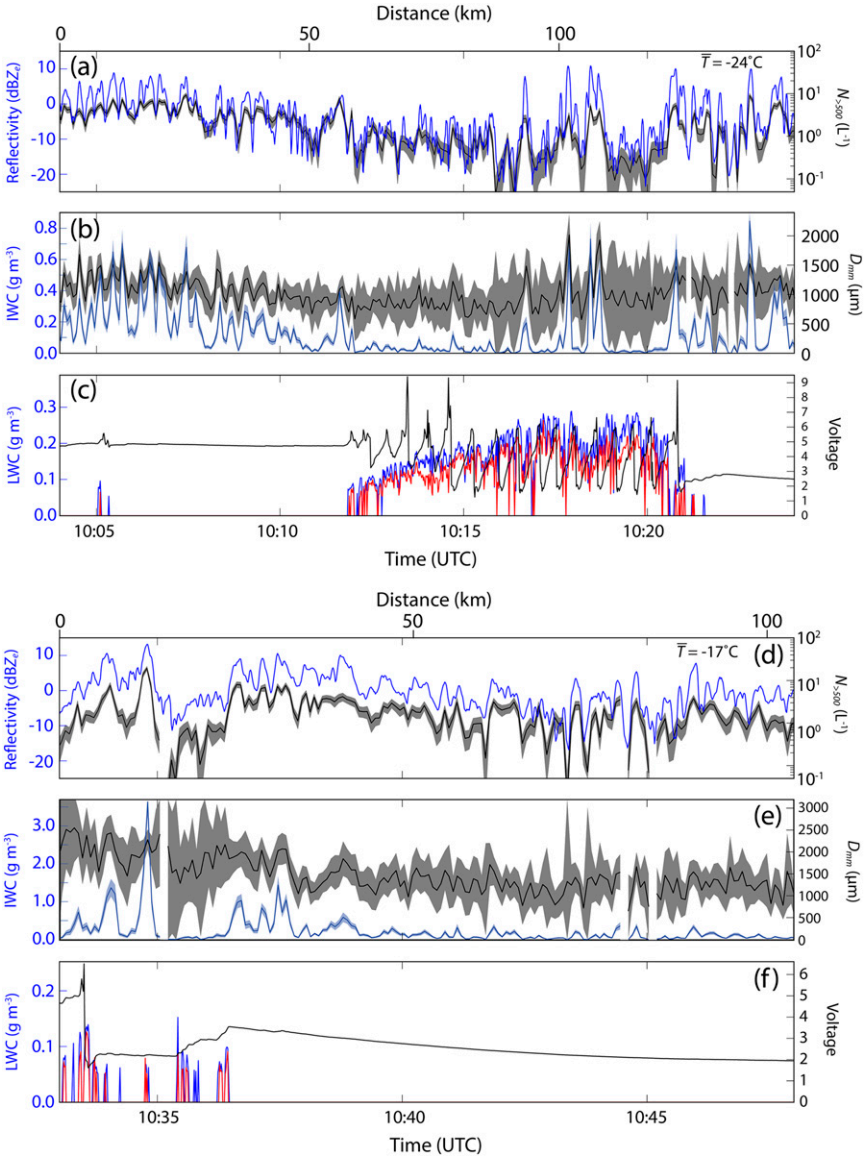

FIG. 8. Time series of (a) Z_e (blue, left axis) and $N_{>500}$ (black, right axis); (b) IWC (blue, left axis) and D_{mm} (black, right axis); and (c) King (blue) and PVM (red) LWC > 0.05 g m^{-3} (left axis), and RICE voltage (black, right axis), for the 3.5-km-altitude flight leg, valid for 1004–1024 UTC 15 February 2010. (d)–(f) The same parameters for the 2.6-km-altitude flight leg, valid for 1033–1048 UTC 15 February 2010. Shading around the $N_{>500}$, IWC, and D_{mm} values indicates fractional uncertainty in measurements based on $p^{0.5}$.

with Figs. 10j–l showing measurements for the 2.6-km leg. Heavily rimed particles are visually evident at 3.5-km altitude, some identifiable as branching plates or dendrites, confirming riming is at least partially responsible for the larger and more massive particles evident in Figs. 5, 6, and 8. Rimed particles were observed in both ice- and mixed-phase regions as shown in Fig. 10a (ice-phase only) and Figs. 10b and 10c (for LWCs near or above 0.1 g m^{-3}). Similarly, rimed particles were often present at 2.6-km altitude, although with many large dendritic crystals and aggregates also evident early in the leg when the largest LWCs were encountered (Figs. 10e,f). Rimed particles became more visually dominant from approximately 1038 UTC through the end of the segment (Fig. 10d), even in ice-phase conditions. Along both the 3.5- and 2.6-km legs, little difference was evident in the habits encountered based on position within or between GCs; the primary difference was in the size and number of larger particles (e.g., Figs. 10b,c compared with Figs. 10h,i). The presence of rimed particles in ice-phase

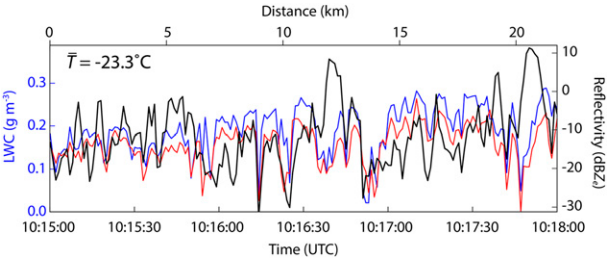

FIG. 9. Time series measurements of Z_e (black), as well as King (blue) and PVM (red) LWC valid for 1015–1018 UTC 15 February 2010.

regions and the similarity in habits within and between the GCs (as was evident for the higher-altitude legs) again indicates the importance of turbulent mixing throughout the GC regions.

The differences in Z_e, $N_{>500}$, IWC, $D_{\rm mm}$, and $N(D)$ within and between GCs for the 14–15 February 2010 cyclone were all consistent with enhanced ice nucleation and growth within the generating cells, with the cells at lower altitudes tending to have lower number concentrations but larger particles compared to those at higher altitudes. The differences between the GCs occurring at higher and lower altitudes could largely be related to the production of SLW in the GC convection occurring at higher temperatures. Particle habits (predominantly rosettes and columns at lower temperatures, as well as dendritic forms at higher temperatures) were consistent with depositional growth in environments characterized by enhanced ice supersaturation (e.g., Bailey and Hallett 2009). Because of the SLW encountered in the GCs between −15° and −25°C, heavily rimed particles also occurred along the lower-altitude flight legs, explaining the larger IWC and $D_{\rm mm}$ encountered along those legs. The particle imagery as well as the averaged $N(D)$, which became broader at the highest temperatures, also support aggregation as a growth mechanism at higher temperatures in some instances. The net effect of these additional enhanced growth processes within the GCs was evident in the largest Z_e values that were measured along the lower-altitude legs.

4. Statistics of full GC dataset

a. Description and general properties

In situ observations were made of GCs during 12 research flights across 11 cyclones during the PLOWS campaign. These flights covered a more extensive range of environmental conditions than those sampled on 15 February 2010. Table 1 summarizes the dataset in terms of average altitude and temperature for each pass through GC regions. Over the entire project,

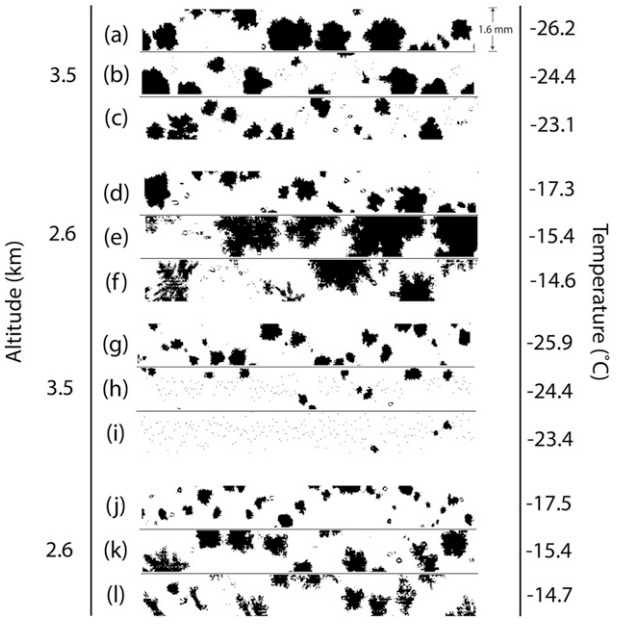

FIG. 10. As in Fig. 7, but corresponding to the flight segments in Fig. 8 for particles sampled at (a) 1004:06, (b) 1013:42, (c) 1016:38, (d) 1044:07, (e) 1034:48, (f) 1033:22, (g) 1004:19, (h) 1013:40, (i) 1016:28, (j) 1044:35, (k) 1034:28, and (l) 1033:01 UTC. (a)–(f) Measurements within GC cores and (g)–(l) measurements at Z_e minima between GCs.

approximately 5.9 h of flight time was spent within GC regions (including measurements in and between cells). Most passes consisted of several minutes near the cloud top, with most of the lengthier passes (10 min or longer—for example, those described in section 3) taking place during three research flights: two sampling a cyclone on 8–9 February 2010 and the 15 February 2010 flight (see also Rosenow et al. 2014). As in section 3, measurements were partitioned using Z_e to define whether data were obtained within or between GCs. Statistics of microphysical properties were again calculated separately for measurements encompassing Z_e peaks (the GC cores) and outside Z_e peaks (between GC cores).

Figure 11 summarizes the range of $D_{\rm mm}$ and IWC (indicated by the color shading) sampled relative to air temperature within all GC regions (both within and between GC cores), with the measurements averaged over 5-s intervals. Generating cells were sampled between −10° and −55°C, with most measurements made between −15° and −30°C. Restrictions on aircraft operations due to aircraft icing limited the number of measurements in cloud for $T > -15$°C. For $T < -30$°C, most measurements had $D_{\rm mm} < 800\,\mu$m and IWC $< 0.15\,{\rm g\,m^{-3}}$, while larger $D_{\rm mm}$ (above 2000 μm) and IWC (near or above $0.7\,{\rm g\,m^{-3}}$) occurred at T between −30°

TABLE 1. PLOWS flight legs contributing to GC dataset, sorted by average temperature. Note that measurements within 105 m of cloud top are assigned a depth of 0 m.

Date	Length (s)	Avg alt (km)	Avg temp (°C)	Avg depth in cloud (m)
15 Feb 2010	346	7.3	−51.1	326
15 Feb 2010	689	7.3	−51.1	221
15 Feb 2010	178	6.8	−45.8	574
15 Feb 2010	478	6.7	−45.2	0
15 Feb 2010	483	6.7	−45.2	832
15 Feb 2010	194	6.8	−44.5	1135
15 Feb 2010	449	6.8	−44.3	1063
15 Feb 2010	259	6.8	−44.2	534
15 Feb 2010	214	6.8	−44.1	189
15 Feb 2010	196	6.8	−43.8	1084
15 Feb 2010	388	6.4	−42.5	1038
26 Feb 2010	515	7.0	−38.5	225
26 Feb 2010	285	7.0	−38.1	363
26 Feb 2010	259	6.7	−37.2	57
15 Feb 2010	320	4.6	−31.1	560
14 Dec 2009	245	6.4	−31.0	108
8 Feb 2010	134	4.1	−29.4	93
26 Feb 2010	91	5.8	−28.9	489
8 Feb 2010	1108	4.1	−28.3	686
15 Feb 2010	106	4.0	−28.1	276
2 Mar 2010	214	6.0	−28.0	126
15 Feb 2010	39	3.5	−27.6	0
8 Feb 2010	64	3.8	−27.1	603
8 Feb 2010	104	3.9	−26.6	794
2 Mar 2010	175	5.7	−25.5	118
2 Mar 2010	216	5.7	−25.3	78
2 Mar 2010	133	5.7	−25.3	330
8 Feb 2010	221	3.8	−25.2	1033
22 Feb 2010	88	5.9	−24.8	244
16 Jan 2010	67	6.6	−24.6	106
8 Feb 2010	302	3.8	−24.4	413
15 Feb 2010	1528	3.5	−24.4	275
8 Feb 2010	43	3.9	−24.1	530
8 Feb 2010	1055	3.8	−23.7	367
9 Feb 2010	152	2.9	−23.2	56
30 Jan 2010	74	5.8	−22.9	548
9 Feb 2010	1031	3.2	−22.9	293
30 Jan 2010	240	5.8	−22.7	302
9 Feb 2010	572	2.9	−22.5	379
14 Dec 2009	132	5.1	−21.8	842
22 Feb 2010	114	5.2	−21.6	1760
26 Feb 2010	51	4.9	−21.2	0
26 Feb 2010	352	4.8	−21.1	18
26 Feb 2010	178	4.8	−21.0	220
9 Feb 2010	218	2.3	−20.0	220
21 Feb 2010	231	5.2	−19.7	236
30 Jan 2010	91	5.3	−19.6	0
9 Feb 2010	1093	2.9	−19.1	461
26 Feb 2010	61	4.5	−18.8	46
14 Dec 2009	599	4.4	−18.6	0
15 Feb 2010	238	2.6	−18.6	1269
8 Feb 2010	164	2.9	−18.5	1289
15 Feb 2010	80	2.8	−18.5	162
14 Dec 2009	123	4.5	−18.1	0
14 Dec 2009	127	4.5	−18.0	0
30 Jan 2010	105	5.1	−18.0	0
14 Dec 2009	474	4.5	−17.3	10

TABLE 1. (*Continued*)

Date	Length (s)	Avg alt (km)	Avg temp (°C)	Avg depth in cloud (m)
30 Jan 2010	19	4.5	−16.5	0
26 Feb 2010	95	4.3	−16.4	1
15 Feb 2010	913	2.6	−16.2	966
30 Jan 2010	161	4.8	−16.1	0
15 Feb 2010	219	2.6	−16.1	288
9 Dec 2009	118	4.5	−16.0	751
30 Jan 2010	174	4.5	−16.0	118
9 Mar 2010	246	5.3	−15.3	16
9 Mar 2010	266	5.3	−15.0	75
30 Jan 2010	311	4.5	−14.6	0
2 Dec 2009	79	5.0	−14.4	1495
9 Dec 2009	134	4.3	−14.2	791
14 Dec 2009	49	3.9	−13.9	196
14 Dec 2009	114	3.9	−13.7	60
14 Dec 2009	58	3.7	−13.2	228
30 Jan 2010	91	4.2	−13.0	278
9 Dec 2009	305	3.9	−12.0	282
30 Jan 2010	103	3.9	−11.2	818

and −15°C. The largest values of both parameters occurred for T near −15°C.

The statistical distributions of microphysical parameters within and between GCs are summarized in Fig. 12, which shows box-and-whisker plots of the median and 5th, 25th, 75th, and 95th percentiles of Z_e, $N_{>500}$, IWC, and D_{mm} in 10°C intervals centered at −11°, −21°, −31°, −41°, and −51°C. The specific temperature intervals used here were chosen based on the distribution of measured temperatures such that each interval had sufficient samples for statistical analysis. Overall, the most consistent trend with respect to temperature was an increase in the statistical range of the measurements for cells occurring at the highest temperatures. While $N_{>500}$ values tended to decrease at higher temperatures, the largest values of the other parameters (particularly IWC and D_{mm}) were consistently observed in cells at the higher end of the temperature range. More distinct signatures were generally evident for measurements within cells compared to between them. The median Z_e at each temperature are ~5 dBZ_e larger for measurements made within the GC cores compared to outside, and the range of Z_e increases with increasing T (Fig. 12a). While the larger Z_e values within the GCs were expected, given that the cell locations were defined using that parameter, the Z_e statistics are shown here primarily to summarize the range of values with respect to temperature. The median and statistical percentiles of $N_{>500}$ (Fig. 12b) were generally ~1.3–3 times larger within cell cores, averaging 1.9 times larger overall.

To account for the unequal sample sizes in the T intervals, bootstrap resampling (Efron and Tibshirani 1993; McFarquhar and Heymsfield 1997), a modified Monte Carlo technique, was used to estimate the variability of the statistical percentiles. The standard deviations of the statistical $N_{>500}$ percentiles for the resampled data were relatively small, averaging 0.7 L^{-1} within the GC cores and 0.2 L^{-1} between them, providing confidence that the observations in each T interval are a good representation of the true population. Median and statistical IWC percentiles within cell cores averaged 2.2 times larger (Fig. 12c), and D_{mm} averaged 1.1 times larger overall (Fig. 12d), compared to measurements between cells. The range of the statistical percentiles increased for both variables as temperature increased, and their standard deviations for the resampled data were again small, averaging 0.06 g m^{-3} and ~50 μm within the GC cores and 0.01 g m^{-3} and ~20 μm between them.

It should be noted that particles with $D < 500\,\mu$m contribute to the total IWC. The IWC calculated for $150 < D < 500\,\mu$m, using standard corrections for particle shattering (Jackson et al. 2014), contributed ~17% on average to the total IWC, with the largest average contribution (~55%) occurring in GC cores at $T < -36$°C and lower contributions elsewhere. Therefore, small particles can make important contributions to the total IWC, particularly in GCs occurring at lower temperatures.

The exceptions in the trend of larger median values within cell cores were for the in situ measurements ($N_{>500}$, IWC, and D_{mm}) at $T = -11° \pm 5$°C. While Z_e values were still enhanced within the cells, smaller median values of the three parameters were evident compared to measurements between cells. However, if the mean rather than the median was used, similar

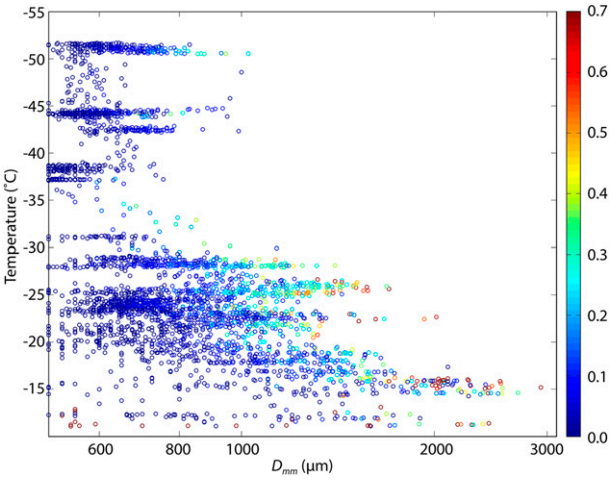

FIG. 11. All T–D_{mm} data pairs within generating cell regions, using 5-s averaging. Color scale indicates IWC (g m^{-3}).

signatures would be noted; for example, the mean $N_{>500}$ at −11° ± 5°C was larger within GCs than between them, even though the median was slightly smaller. In addition, the 75th–95th percentiles of $N_{>500}$ and IWC were larger for measurements within GCs at −11° ± 5°C, while the 95th percentiles for D_{mm} indicate that large particles were present both within and between cells.

Figures 13a and 13b show the measurements of Z_e versus D_{mm}, with color shading indicating $N_{>500}$ values, for data within (Fig. 13a) and between (Fig. 13b) cell cores. Although there is considerable scatter, there is larger Z_e on average for a given D_{mm} within the cores compared to between them. Consequently, larger $N_{>500}$ must be present within the cell cores. Similarly, when the Z_e–D_{mm} pairs are sorted by IWC (Figs. 13c,d), larger IWCs are evident within the cores, as suggested by the larger Z_e for a given D_{mm}. Figure 14 shows $N(D)$ averaged in 10°C intervals, partitioned according to whether data were collected within (solid) or between (dashed) cell cores. Similar to the case study (Fig. 6), the concentrations were consistently enhanced within the cores at all temperatures by an average of 1.7 times, and up to a factor of 3.3. The ratio was maximized for D between ~1500 and 2000 μm. Again, the distribution became flatter for larger T. The maximum particle diameter increased from ~2000 to 6000 μm over the range of measured T, from −51° to −11°C.

b. *Supercooled liquid water and ice- versus mixed-phase conditions*

The range of conditions sampled in GCs included both ice-phase and mixed-phase environments. As in section 3, it was assumed that for LWC > 0.05 g m^{-3}, the aircraft

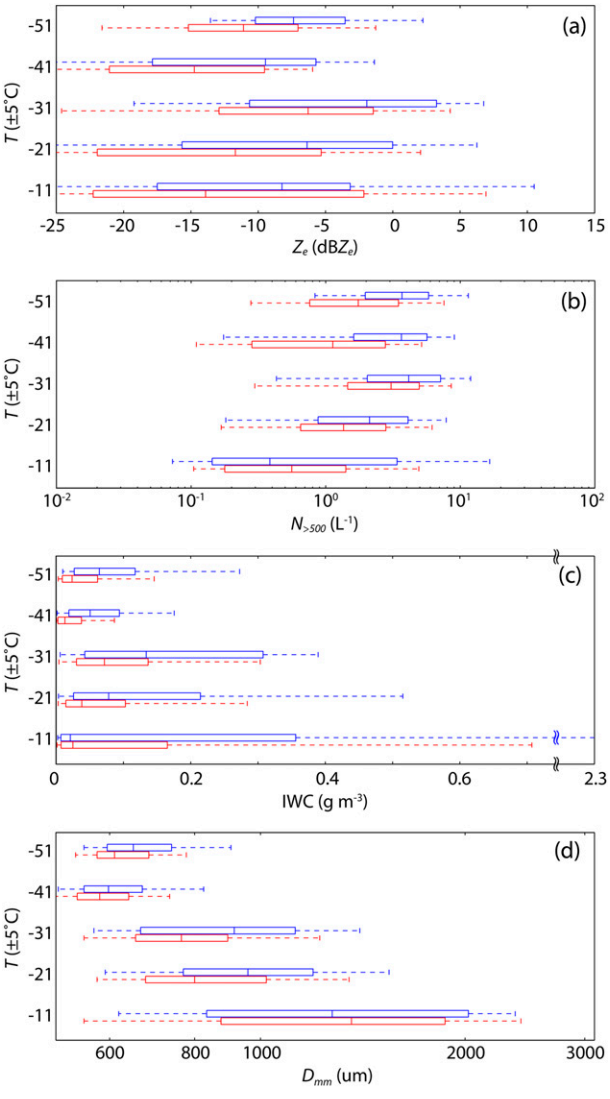

FIG. 12. As in Fig. 5, but showing statistics for: (a) Z_e, (b) $N_{>500}$, (c) IWC, and (d) D_{mm} in 10°C intervals for the entire generating cell dataset. The median and percentiles in blue are for measurements within GC cores, and the median and percentiles in red are between GCs.

was in mixed-phase conditions; only a few brief sampling periods occurred when ice crystals were not detected simultaneously when SLW was present. Although this threshold precludes the inclusion of some periods with minimal LWC, it minimizes the risk of erroneously including measurements where SLW may not have been present. Figure 15a summarizes the measured LWCs with respect to T using data at 1-s resolution. Supercooled water was detected at T as low as −31.4°C, though nearly all instances occurred for $T \geq -28$°C. If convective updrafts were sufficient to produce liquid droplets at the lower temperatures, they likely underwent rapid nucleation and froze. When the LWC was

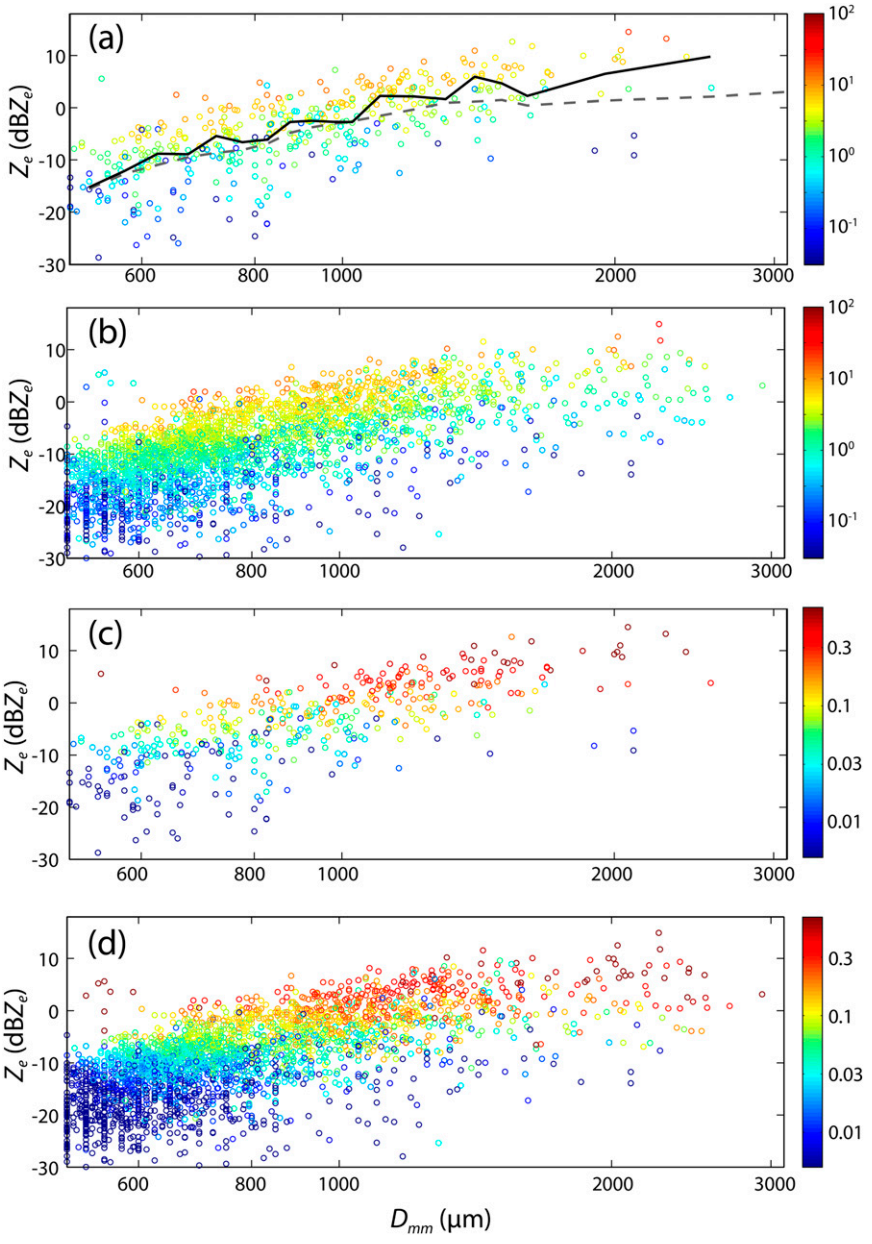

FIG. 13. (a),(b) Z_e–$D_{\rm mm}$ data pairs, with $N_{>500}$ (L^{-1}) indicated by color shading, for measurements (a) within and (b) between GC cores, using 5-s averaging. (c),(d) The same data pairs, but with IWC ($g\,m^{-3}$) indicated by color shading. The lines in (a) indicate the median Z_e values with respect to $D_{\rm mm}$, for measurements within (black) and between (dashed gray) GC cores.

greater than $0.05\,g\,m^{-3}$, the median value increased slightly from approximately 0.09 to $0.12\,g\,m^{-3}$ with increasing temperature, with 95th-percentile LWC values increasing from 0.14 to $0.28\,g\,m^{-3}$. Note that the 95th-percentile values were near or above $0.20\,g\,m^{-3}$ for much of the temperature range. Again, the standard deviations of the LWC percentiles using bootstrap resampling were quite small, generally at or below $0.01\,g\,m^{-3}$. Supercooled water was encountered both within and between cell cores, implying that mixing due to the turbulent environment acts to distribute SLW throughout the GC region. The LWC percentiles were $\sim 0.04\,g\,m^{-3}$ larger within cell cores compared to measurements between them, and ~26% of all measurements within GC cores at $T \geq -31.4$°C contained LWC $> 0.05\,g\,m^{-3}$, compared to ~18% of measurements between cores.

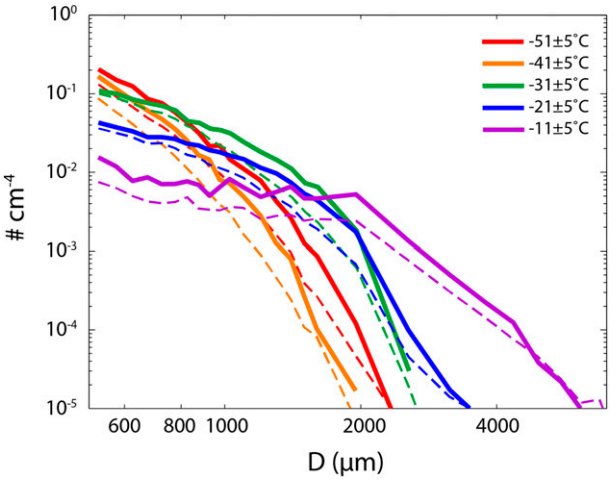

FIG. 14. As in Fig. 6, but $N(D)$ averaged in the 10°C intervals indicated in Fig. 12 for the entire generating cell dataset.

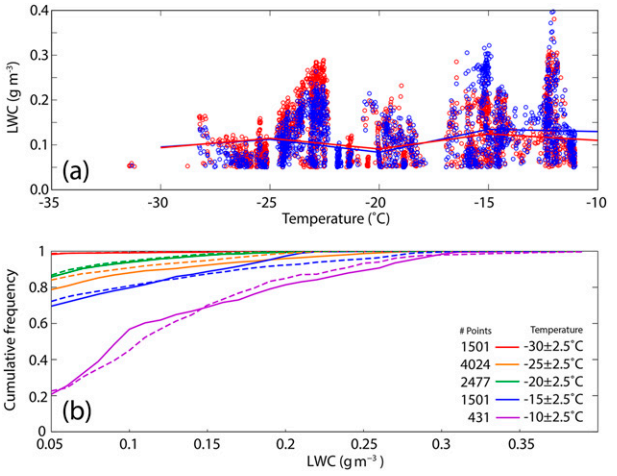

FIG. 15. (a) Scatterplot of King (blue) and PVM (red) LWC > 0.05 g m^{-3} with respect to T, with solid lines indicating median values in 5°C intervals; (b) cumulative distribution functions showing fraction of PVM (solid) and King (dashed) measurements at or below the x-axis values, along with total number of 1-s-resolution measurements in each T interval.

Cumulative distribution functions of SLW's presence with respect to temperature are shown in Fig. 15b for all measurements in cloud within GC regions, along with the total number of observations (at 1-s resolution) in each temperature interval. For GCs at −10° ± 2.5°C, SLW was present (LWC > 0.05 g m^{-3}) in nearly 80% of observations, although the number of measurements was smallest within this temperature interval. The largest LWCs (~0.4 g m^{-3}) were measured in this temperature range. The percentage of measurements with SLW present decreased for the observations made at lower temperatures, with ~30% of measurements containing SLW for −15° ± 2.5°C, and 15%–20% of observations between −17.5° and −27.5°C containing SLW. Liquid water was only directly measured in a small number of observations at $T < -27.5$°C.

Figure 16a shows the measured LWCs with respect to distance below radar-derived cloud top, again for data at 1-s resolution. Note that some uncertainty exists in the calculated distance when the aircraft was very close to cloud top. Because no radar data are available within 105 m of the aircraft, the distance below cloud top in these instances was set to 0 m (evident in the measurements aligned vertically along the left edge of Fig. 16a) rather than a negative value corresponding to the nearest usable radar data below the aircraft. The median and 95th-percentile LWC values were ~0.13 and 0.26 g m^{-3}, respectively, for measurements within 0.33 km of cloud top. Deeper within the cloud (0.33–1.33 km below cloud top), the median and 95th-percentile LWC values averaged ~0.08 and 0.16 g m^{-3}. Similar LWCs were encountered further below cloud top, but the total number of measurements was much smaller, with ~95% of measurements made within 1.33 km of cloud top. Overall, the standard deviation of the percentiles using bootstrap resampling averaged ~0.01 g m^{-3}. Figure 16b shows cumulative distribution functions of LWC with respect to depth in cloud. Approximately 25% of measurements within 0.33 km of cloud top featured LWC > 0.05 g m^{-3}, and the largest LWCs were encountered at these depths. Deeper within cloud (0.33–1.33 km), LWC > 0.05 g m^{-3} occurred in less than 10% of observations. The SLW frequency increased again deeper within cloud at higher temperatures, though again, the number of observations was much smaller at these depths, and the increase may not be statistically significant.

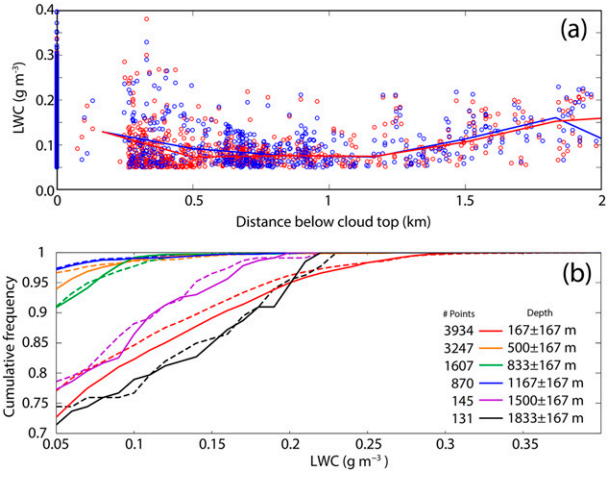

FIG. 16. As in Fig. 15, but SLW measurements shown with respect to radar-derived cloud top, with median and cumulative distribution function calculations using 0.33-km intervals.

The relationship between Z_e and D_{mm} in all GC cores is shown in Fig. 17 for measurements segregated between ice-phase and mixed-phase conditions, with $N_{>500}$ (Figs. 17a,b) and IWC (Figs. 17c,d) indicated by color shading. Ice-phase measurements for $D_{mm} < \sim 1200\,\mu$m exhibit larger $N_{>500}$ and IWC for a given D_{mm}, resulting in generally larger Z_e. Figure 18 shows temperature-averaged $N(D)$ within GCs for ice-phase (solid) and mixed-phase (dashed) conditions. For $T < -16$°C, $N(D)$ averaged 1.9 times larger in ice-phase than in mixed-phase conditions for $D < 2000\,\mu$m. For larger diameters, the $N(D)$ values averaged 1.7 times larger in ice-phase compared to mixed-phase for $T = -31° \pm 5$°C, but averaged 2.5 times larger and extended to larger particles ($D \approx 4000\,\mu$m) in mixed-phase conditions for $T = -21° \pm 5$°C. This is consistent with SLW becoming increasingly important to ice growth processes for GCs occurring at higher temperatures, with a decrease in small particle concentrations coincident with increasing concentrations of large particles in the presence of SLW for T near −21°C. Pure ice-phase conditions in the GC regions were almost nonexistent for $T > -16$°C; while the ice-phase $N(D)$ values show enhanced concentrations compared to the mixed-phase measurements for this temperature interval, they only incorporate a small number of measurements. The average mixed-phase $N(D)$ was similar to the corresponding temperature-averaged $N(D)$ within GCs in Fig. 14, with particles growing to ~6000 μm in these environments.

c. *Potential uncertainties and robustness of results*

Several factors contribute uncertainties to the quantitative results presented and, in particular, to the IWCs calculated above. Although the shattering of ice crystals on the standard 2D-C probe tips used during PLOWS artificially generates small ice crystals, Jackson and McFarquhar (2014) showed that uncertainties in IWC from shattering are smaller than uncertainties associated with estimating particle mass from a two-dimensional cross section of a particle image. Such estimations assume an effective density, which in reality depends on the particle characteristics (e.g., shape, amount of riming) and can vary by environment. While bulk mass content measurements and higher-resolution particle imagery (e.g., from a Cloud Particle Imager) could have reduced uncertainties in the derived IWC, existing measurements of crystal morphology did not show large changes in habit or riming fraction within or between GCs. Thus, it is unlikely that major differences in parameterizations to estimate IWC from $N(D)$ existed within or between GCs, so the qualitative differences derived in IWCs in and out of GCs are likely robust.

Additionally, because of the range of GC sizes and intensities, the Z_e thresholds used to identify GC cores and the temporal averaging used for the in situ measurements affect how the cell cores are separated from surrounding regions. To evaluate the results' sensitivity to the classification criteria, the statistics were also calculated using a variety of Z_e thresholds and averaging times. The signatures were broadly similar when relative Z_e maxima of 3 dB or greater were used to identify GC cores. Enhancements for $N_{>500}$ and IWC were typically within a factor of ~0.9–1.3 to those described above, generally increasing for larger Z_e thresholds. The largest exceptions were for measurements at $T > -16$°C using a 3-dB threshold, with smaller enhancements for $N_{>500}$, IWC, and D_{mm} noted, with D_{mm} in general being less sensitive to the threshold used. No completely consistent trend was apparent with respect to averaging time, but weaker enhancements became more common with longer averaging times (particularly above 7 s), suggesting that the longer averaging time resulted in data from the cores and environment between the cores being included in the same average. Overall, while some uncertainties do exist in separating GC cores from surrounding regions, the results consistently characterized GCs as providing environments favorable for enhanced ice production and growth relative to surrounding regions.

5. Discussion and conclusions

Data were collected using in situ cloud microphysics instruments within and outside of cloud-top generating cells (GCs) in the comma head regions of eleven cold-season continental cyclones during the Profiling of Winter Storms (PLOWS) field campaign. The data were analyzed to quantify how the size, shape, and phase distributions of cloud particles varied inside and outside of the GCs, with the cell location defined based on radar reflectivity maxima, as measured by the University of Wyoming Cloud Radar (WCR). This research builds upon previous studies in that data acquired through GCs in 11 cyclones at temperatures between −10° and −55°C were used to considerably expand the number of cases analyzed in a much wider range of conditions. The current study also takes into account the impact of particle shattering artifacts on derived microphysical properties and uses statistical analyses to demonstrate the differences of microphysical properties inside and outside of the GCs. Detailed analyses of one cyclone containing GCs at two separate temperature ranges also provided information about the physical processes responsible for ice crystal properties within the GCs. The principal conclusions of this study are as follows:

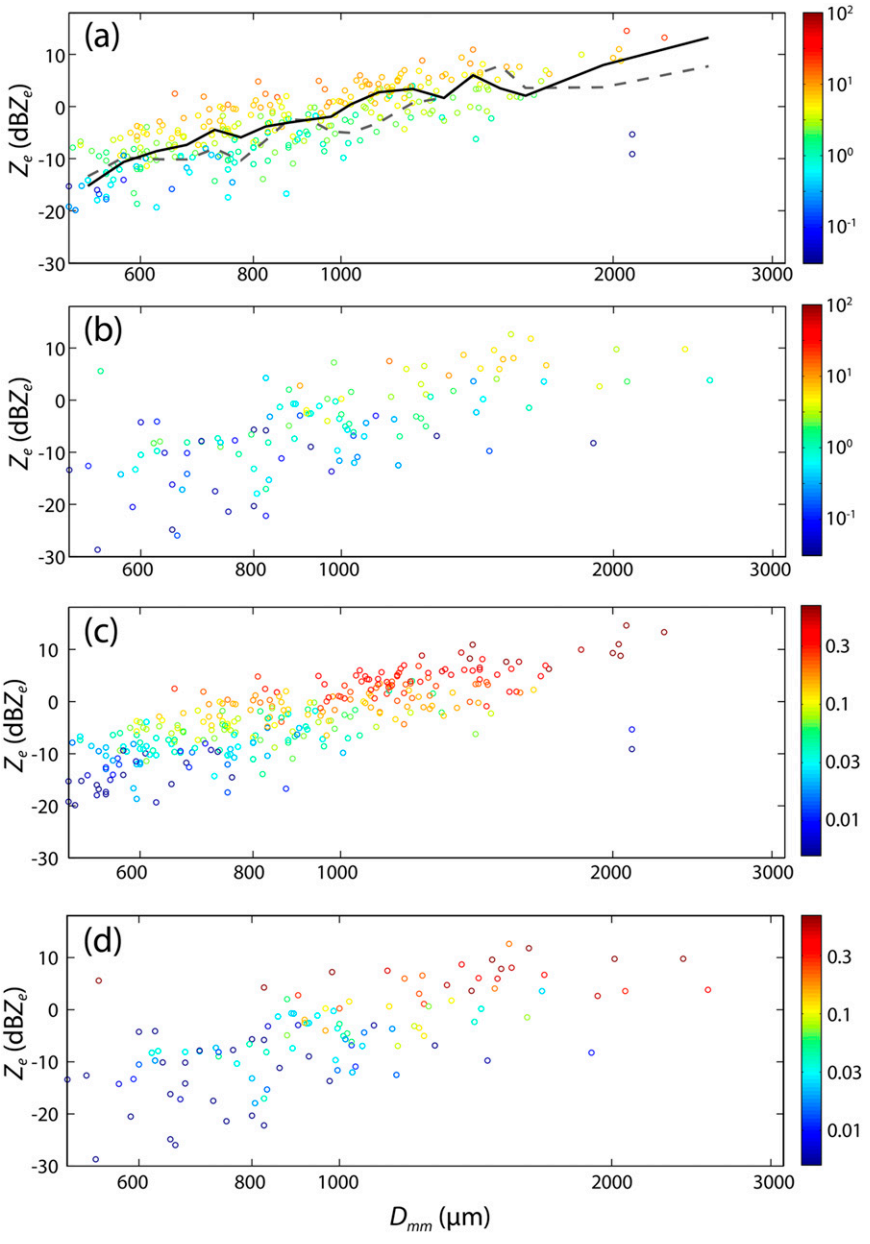

FIG. 17. As in Fig. 13, except showing only measurements within GC cores. (a),(c) Ice-phase measurements and (b),(d) mixed-phase measurements. The lines in (a) indicate the median Z_e values with respect to D_{mm} for measurements within ice-phase (black) and mixed-phase (dashed gray) conditions. In (a),(b), color shading denotes $N_{>500}$ (L^{-1}), and in (c),(d), color shading denotes IWC ($\mathrm{g\,m}^{-3}$).

1) The number concentrations of particles with maximum dimension $D > 500\,\mu$m $N_{>500}$ were ~1.3–3 times larger (average 1.9) inside GCs compared to outside. The derived ice water content (IWC) and median mass diameter D_{mm} averaged 2.2 and 1.1 times larger in the cells, with the range of their 95th percentiles increasing with increasing temperatures. The enhanced $N_{>500}$ values are consistent with more ice nuclei activated in convective updrafts, with the increased IWC and D_{mm} suggesting environments favorable for particle growth in the GCs. Approximate estimates of IWC for particles with $150 < D < 500\,\mu$m suggested an average overall contribution of ~17% to the total IWC but up to 55% in GCs at $T < -36$°C.
2) The average number distribution functions $N(D)$ featured larger concentrations within the cells than those outside by an average factor of 1.7 and up to

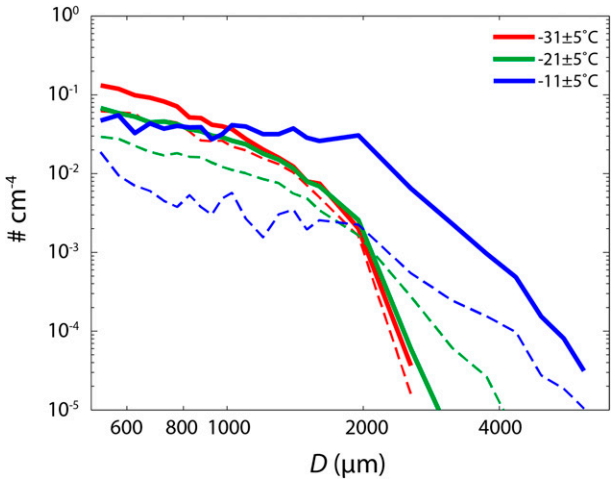

FIG. 18. As in Fig. 14, but for ice-phase (solid) and mixed-phase (dashed) measurements for the entire generating cell dataset.

a factor of 3.3 for all temperatures, with maximum differences for $\sim 1500 < D < 2000\,\mu$m.

3) Supercooled liquid water (SLW) was directly measured for $T \geq -31.4$°C, with nearly all measurements of SLW made for $T \geq -28$°C. When SLW was present, the median water content (LWC) increased slightly from approximately 0.09 to 0.12 g m^{-3} between −32° and −10°C, with 95th-percentile LWC values increasing from 0.14 to 0.28 g m^{-3}. Over this temperature range, SLW was directly measured in 26% of observations within GCs and 18% of observations between the cells, and the median and 95th-percentile LWC values averaged ~0.04 g m^{-3} larger inside compared to outside the GCs. The median and 95th-percentile LWCs were ~0.13 and 0.26 g m^{-3} for measurements within 0.33 km of radar-defined cloud top, decreasing to ~0.08 and 0.16 g m^{-3}, respectively, from 0.33 to 1.33 km below cloud top.
4) At lower temperatures, bullet rosettes were the most common identifiable habit, with columns and plates sometimes evident. With increasing temperature, rimed particles became increasingly common, and dendrites and aggregates were sometimes present, the latter being observed in several PLOWS cases for T between −15° and −20°C. The effect of aggregation was also seen in that averaged $N(D)$ for $D <$ ~2000 μm became flatter with lower concentrations and extended to increasingly large particle sizes at higher temperatures. Similar habits were identified inside and outside of GCs, and rimed particles were observed both in ice- and mixed-phase regions, with the primary differences being the size and number of the larger particles.
5) For $D_{mm} <$ ~1200 μm, measurements in the ice-phase exhibited larger $N_{>500}$ and IWC for a given D_{mm}, and larger Z_e were also typical for a given D_{mm} in ice-phase conditions than in mixed-phase, because of the larger $N_{>500}$. Correspondingly, averaged $N(D)$ in ice-phase conditions showed larger concentrations than in mixed-phase conditions for small particles by an average factor of 1.9 for $D < 2000\,\mu$m, with the difference decreasing toward $D = 2000\,\mu$m. The concentrations for $D > 2000\,\mu$m averaged 1.7 times larger in ice-phase compared to mixed-phase for $T <$ −26°C, but for $T = -21° \pm 5$°C, the averaged mixed-phase $N(D)$ averaged ~2.5 times larger than in ice-phase. Above −16°C, nearly all measurements were mixed-phase, with the averaged $N(D)$ flatter and extending to larger particle sizes ($D \approx 6000\,\mu$m).

The PLOWS measurements are broadly consistent with past studies (e.g., Houze et al. 1981; Wolde and Vali 2002; Evans et al. 2005; Ikeda et al. 2007; Crosier et al. 2014), although the degree of enhancement is reduced compared to some of those studies, as the PLOWS analyses incorporated a much larger range of environmental conditions and took into account the effects of particle shattering on variables derived from in situ measurements. Additionally, the PLOWS measurements included observations of SLW occurring in GC regions over a larger range of temperatures than in the past studies. The measured LWCs were similar to those observed by Houze et al. (1981), Rauber and Grant (1986), and Ikeda et al. (2007) but larger than those observed by Evans et al. (2005) in newly formed convective cells. The difference is attributed to the fact that a much larger range of cell lifetimes was sampled during PLOWS. As in Field et al. (2004) and Ikeda et al. (2007), SLW was measured both within and between convective cores. Unlike those studies, which concluded that enhanced ice concentrations preferentially depleted the SLW within the convection, the LWCs in this study were statistically larger and encountered more frequently within the GC cores.

The presence of SLW in the GCs is important because of its major impacts on both primary ice nucleation and particle growth processes (e.g., Rauber and Tokay 1991; Westbrook and Illingworth 2011). Supercooled water's production enhances primary ice nucleation by allowing multiple nucleation processes (deposition, condensation, and contact) to take place, and its consistent presence in the PLOWS dataset implies the production of considerable ice supersaturations over a large temperature range. The resulting environments are favorable for enhanced ice growth at high supersaturations, consistent with the observed IWC, D_{mm}, and $N(D)$ signatures. The measurements were consistent with SLW becoming increasingly important to growth processes in GCs occurring at higher temperatures, and SLW was

nearly ubiquitous for $T > -16$°C. The resulting enhanced ice growth was apparent in that heavily rimed particles were commonly present in particle imagery, with larger particles produced in mixed-phase rather than ice-phase environments for $T > -26$°C.

The small horizontal scales (~1.5–2 km or less) of the GCs, their turbulent nature (evident in the vertical radial velocity profiles in Fig. 3), and their close proximity to other regions suggest that mixing and entrainment/detrainment occurred between the regions (cf. McFarquhar et al. 2011). Several characteristics were consistently present in the PLOWS observations showing the influence of mixing, including the presence of SLW within and between GCs, the similarity of habits within and between cells, and the appearance of rimed particles even outside of GCs in ice-phase conditions. These characteristics were consistently noted regardless of the exact definitions used to identify the cells. For example, the presence of SLW was noted even at Z_e minima that would not be identified as cells (e.g., Fig. 9), as were the habit signatures described above. Therefore, while the uncertainties in separating out GC cores impact the results, the measurements also support the importance of turbulent mixing due to convective air motions acting to lessen the observed differences between the cells and surrounding regions.

The PLOWS observations help to define the microphysical processes that occur within cloud-top GCs and how these depend on the cells' environment. However, the GCs are only part of a larger-scale process controlling precipitation development in that they commonly act to seed ice particles into stratiform environments, which provide conditions favorable for additional particle growth as the particles fall (Rosenow et al. 2014). While many previous studies (e.g., Houze et al. 1976; Matejka et al. 1980; Herzegh and Hobbs 1980) have identified primary particle growth as occurring below the GC level, the PLOWS observations show significant growth occurring within GCs in some circumstances. For example, large rimed particles, large dendritic crystals, and some aggregates were observed near −17°C in the GC regions of the 14–15 February 2010 cyclone, and particles up to 5–6 mm in maximum dimension were present in the GCs sampled in the PLOWS dataset, particularly for $T = -11° \pm 5$°C. These observations are consistent with the rapid growth of particles at temperatures near −15°C, where the environment is most favorable for the growth of ice at the expense of liquid and where growth by riming is also possible. A subsequent study will supplement the analyses shown here by evaluating the microphysical characteristics and particle growth mechanisms occurring in stratiform regions below GCs and identifying how these relate to the convection present at cloud top.

Acknowledgments. The authors thank the staff at the National Center for Atmospheric Research Environmental Observing Laboratory, particularly Allen Schanot and Jorgen Jensen and the Research Aviation Facility staff for their efforts with the C-130 and the staff of the University of Wyoming King Air facility for their support of the WCR deployment. We thank Major Donald K. Carpenter and the U.S. Air Force Peoria National Guard for housing the C-130 during the project. The assistance of Aaron Bansemer and Jeffrey Stith in interpreting processed 2D-P data is greatly appreciated. The composite radar analysis appearing in Fig. 1 was provided by the Iowa Environmental Mesonet maintained by the Iowa State University Department of Agronomy. Rapid Update Cycle data was provided by the National Climatic Data Center's NOMADS. This work was funded under National Science Foundation Grants ATM-0833828 and AGS-1247404 to the University of Illinois and AGS-1247473 to the University of Wyoming.

APPENDIX

Processing of 2D-P Optical Array Probe Measurements

A comparison of properties derived from the originally processed 2D-C and 2D-P measurements for particles within the probes' typical overlap range (800–1400 μm) revealed that the number distribution functions derived from the 2D-C measurements were consistently larger than those derived from the originally processed 2D-P measurements by up to an order of magnitude. This is a larger discrepancy than expected, given differences in probe resolution, response, and location aboard the aircraft. Typical examples are shown with the blue (2D-C) and red (2D-P) lines in Fig. A1a for a portion of the 15 February 2010 research flight. Although the offset between the measurements was not consistent over any flight, the $N(D)$ from the 2D-C was always substantially larger than that from the 2D-P. The largest discrepancies between the 2D-C and 2D-P were identified where particle sizes were predominantly near the small end of the 2D-P size range. Subsequent investigation of the individual 2D-P photodiode response over every flight revealed uneven activity, with reduced response consistently evident across the center of the photodiode array (Fig. A1b).

While the magnitude of the reduced photodiode response decreased for larger particles, the issue was evident over most of the 2D-P size range. Because of this, the 2D-P measurements were ultimately processed

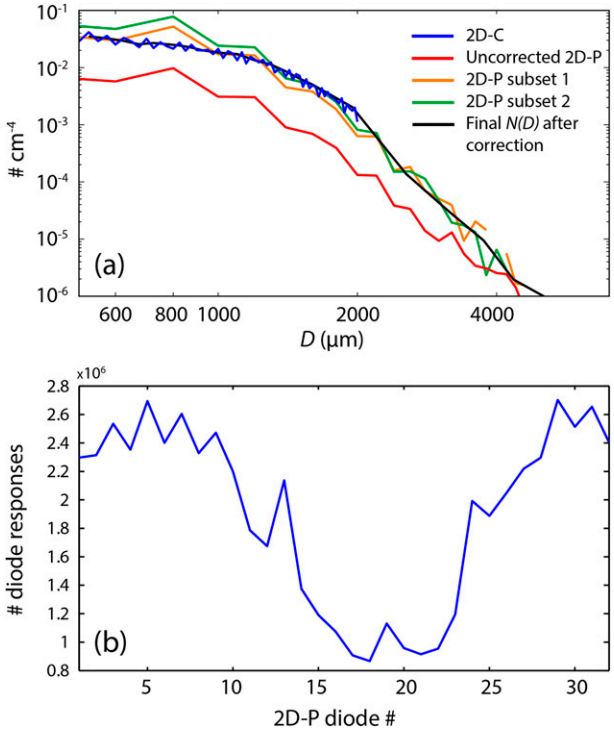

FIG. A1. (a) $N(D)$ averaged from 1004 to 1024 UTC 15 February 2010 for 2D-C (blue) and 2D-P (red) for all photodiodes, using native bin resolution, 2D-P photodiode subsets 1 (orange) and 2 (green), and final combined 2D-C/P distribution (black). (b) Summed individual 2D-P photodiode responses for the 15 February 2010 research flight.

separately for two subsets of the photodiodes, the first 12 and the final 8 surrounding the center of the array, using reconstruction techniques to derive D for particles partially outside the field of view of the photodiode subsets (Heymsfield and Parrish 1978). The measurements from the 2D-P photodiode subsets (e.g., the orange and green lines in Fig. A1a) were much more similar to the 2D-C measurements in the probes' overlapping size range, compared to the measurements using the full photodiode array, and the values varied about the 2D-C measurements as would be expected given the 2D-P's lower resolution. The best agreement was found for environments where ice particles were predominantly of simple shapes (e.g., heavily rimed crystals) that were represented relatively well in the lower-resolution 2D-P measurements. Further, the 2D-P typically undersized more complex particles relative to the 2D-C. Ultimately, a threshold diameter of 2000 μm was used as the cutoff between the 2D-C and 2D-P measurements to provide a balance between the higher-resolution 2D-C data and the more heavily processed 2D-P data. Measurements of particles larger than 2000 μm in diameter were represented by averaging the two 2D-P data subsets. An example of the final, combined $N(D)$ is shown with the black line in Fig. A1a, using larger bin widths relative to the original 2D-C (blue) and 2D-P (red) measurements to incorporate more measurements within each size bin.

REFERENCES

American Meteorological Society, cited 2013: "Generating cell." Glossary of Meteorology. [Available online at http://glossary.ametsoc.org/wiki/generating_cell].

Bader, M. J., S. A. Clough, and G. P. Cox, 1987: Aircraft and dual polarization radar observations of hydrometeors in light stratiform precipitation. *Quart. J. Roy. Meteor. Soc.,* **113,** 491–515, doi:10.1002/qj.49711347605.

Bailey, M. P., and J. Hallett, 2009: A comprehensive habit diagram for atmospheric ice crystals: Confirmation from the laboratory, AIRS II, and other field studies. *J. Atmos. Sci.,* **66,** 2888–2899, doi:10.1175/2009JAS2883.1.

Baker, B., and R. P. Lawson, 2006: Improvement in determination of ice water content from two-dimensional particle imagery. Part I: Image-to-mass relationships. *J. Appl. Meteor. Climatol.,* **45,** 1282–1290, doi:10.1175/JAM2398.1.

Baumgardner, D., and A. Korolev, 1997: Airspeed corrections for optical array probe sample volumes. *J. Atmos. Oceanic Technol.,* **14,** 1224–1229, doi:10.1175/1520-0426(1997)014<1224:ACFOAP>2.0.CO;2.

Bergeron, T., 1950: Über der mechanismum der ausgeibigen Niederschläge. *Ber. Dtsch. Wetterdienstes,* **12,** 225–232.

Boucher, R. J., 1959: Synoptic-physical implications of 1.25-cm vertical-beam radar echoes. *J. Meteor.,* **16,** 312–326, doi:10.1175/1520-0469(1959)016<0312:SPIOCV>2.0.CO;2.

Browning, K. A., 1983: Air motion and precipitation growth in a major snowstorm. *Quart. J. Roy. Meteor. Soc.,* **109,** 225–242, doi:10.1002/qj.49710945911.

Carbone, R. E., and A. R. Bohne, 1975: Cellular snow generation—A Doppler radar study. *J. Atmos. Sci.,* **32,** 1384–1394, doi:10.1175/1520-0469(1975)032<1384:CSGDRS>2.0.CO;2.

Cober, S. G., G. A. Isaac, A. V. Korolev, and J. W. Strapp, 2001: Assessing cloud-phase conditions. *J. Appl. Meteor.,* **40,** 1967–1983, doi:10.1175/1520-0450(2001)040<1967:ACPC>2.0.CO;2.

Crosier, J., and Coauthors, 2014: Microphysical properties of cold frontal rainbands. *Quart. J. Roy. Meteor. Soc.,* **140,** 1257–1268, doi:10.1002/qj.2206.

Cunningham, J. G., and S. E. Yuter, 2014: Instability characteristics of radar-derived mesoscale organization modes within cool-season precipitation near Portland, Oregon. *Mon. Wea. Rev.,* **142,** 1738–1757, doi:10.1175/MWR-D-13-00133.1.

Douglas, R. H., K. L. S. Gunn, and J. S. Marshall, 1957: Pattern in the vertical of snow generation. *J. Meteor.,* **14,** 95–114, doi:10.1175/1520-0469(1957)014<0095:PITVOS>2.0.CO;2.

Efron, B., and R. J. Tibshirani, 1993: *An Introduction to the Bootstrap.* Chapman and Hall, 436 pp.

Evans, A. G., J. D. Locatelli, M. T. Stoelinga, and P. V. Hobbs, 2005: The IMPROVE-1 storm of 1–2 February 2001. Part II: Cloud structures and the growth of precipitation. *J. Atmos. Sci.,* **62,** 3456–3473, doi:10.1175/JAS3547.1.

Field, P. R., R. J. Hogan, P. R. A. Brown, A. J. Illingworth, T. W. Choularton, P. H. Kaye, E. Hirst, and R. Greenaway, 2004: Simultaneous radar and aircraft observations of mixed-phase cloud at the 100 m scale. *Quart. J. Roy. Meteor. Soc.,* **130,** 1877–1904, doi:10.1256/qj.03.102.

Gardiner, B. A., and J. Hallett, 1985: Degradation of in-cloud forward scattering spectrometer probe measurements in the presence of ice particles. *J. Atmos. Oceanic Technol.,* **2,** 171–180, doi:10.1175/1520-0426(1985)002<0171:DOICFS>2.0.CO;2.

Grim, J. A., R. M. Rauber, M. K. Ramamurthy, B. F. Jewett, and M. Han, 2007: High-resolution observations of the trowal–warm-frontal region of two continental winter cyclones. *Mon. Wea. Rev.,* **135,** 1629–1646, doi:10.1175/MWR3378.1.

Gunn, K. L. S., M. P. Langleben, A. S. Dennis, and B. A. Power, 1954: Radar evidence of a generating level for snow. *J. Meteor.,* **11,** 20–26, doi:10.1175/1520-0469(1954)011<0020:REOAGL>2.0.CO;2.

Herzegh, P. H., and P. V. Hobbs, 1980: The mesoscale and microscale structure and organization of clouds and precipitation in midlatitude cyclones. II: Warm-frontal clouds. *J. Atmos. Sci.,* **37,** 597–611, doi:10.1175/1520-0469(1980)037<0597:TMAMSA>2.0.CO;2.

Heymsfield, A. J., and J. L. Parrish, 1978: A computational technique for increasing the effective sampling volume of the PMS two-dimensional particle size spectrometer. *J. Appl. Meteor.,* **17,** 1566–1572, doi:10.1175/1520-0450(1978)017<1566:ACTFIT>2.0.CO;2.

Houze, R. A., Jr., P. V. Hobbs, K. R. Biswas, and W. M. Davis, 1976: Mesoscale rainbands in extratropical cyclones. *Mon. Wea. Rev.,* **104,** 868–878, doi:10.1175/1520-0493(1976)104<0868:MRIEC>2.0.CO;2.

——, S. A. Rutledge, T. J. Matejka, and P. V. Hobbs, 1981: The mesoscale and microscale structure and organization of clouds and precipitation in midlatitude cyclones. III: Air motions and precipitation growth in a warm-frontal rainband. *J. Atmos. Sci.,* **38,** 639–649, doi:10.1175/1520-0469(1981)038<0639:TMAMSA>2.0.CO;2.

Ikeda, K., R. M. Rasmussen, W. D. Hall, and G. Thompson, 2007: Observations of freezing drizzle in extratropical cyclonic storms during IMPROVE-2. *J. Atmos. Sci.,* **64,** 3016–3043, doi:10.1175/JAS3999.1.

Jackson, R. C., and G. M. McFarquhar, 2014: An assessment of the impact of antishattering tips and artifact removal techniques on bulk cloud ice microphysical and optical properties measured by the 2D cloud probe. *J. Atmos. Oceanic Technol.,* **31,** 2131–2144, doi:10.1175/JTECH-D-14-00018.1.

——, and Coauthors, 2012: The dependence of ice microphysics on aerosol concentration in arctic mixed-phase stratus clouds during ISDAC and M-PACE. *J. Geophys. Res.,* **117,** D15207, doi:10.1029/2012JD017668.

——, G. M. McFarquhar, J. Stith, M. Beals, R. Shaw, J. Jensen, J. Fugal, and A. Korolev, 2014: An assessment of the impact of antishattering tips and artifact removal techniques on cloud ice size distributions measured by the 2D cloud probe. *J. Atmos. Oceanic Technol.,* doi:10.1175/JTECH-D-13-00239.1, in press.

Korolev, A. V., E. F. Emery, J. W. Strapp, S. G. Cober, and G. A. Isaac, 2013: Quantification of the effects of shattering on airborne ice particle measurements. *J. Atmos. Oceanic Technol.,* **30,** 2527–2553, doi:10.1175/JTECH-D-13-00115.1.

Langleben, M. P., 1956: The plan pattern of snow echoes at the generating level. *J. Meteor.,* **13,** 554–560, doi:10.1175/1520-0469(1956)013<0554:TPPOSE>2.0.CO;2.

Marshall, J. S., 1953: Precipitation trajectories and patterns. *J. Meteor.,* **10,** 25–29, doi:10.1175/1520-0469(1953)010<0025:PTAP>2.0.CO;2.

Matejka, T. J., R. A. Houze Jr., and P. V. Hobbs, 1980: Microphysics and dynamics of clouds associated with mesoscale rainbands in extratropical cyclones. *Quart. J. Roy. Meteor. Soc.,* **106,** 29–56, doi:10.1002/qj.49710644704.

McFarquhar, G. M., and A. J. Heymsfield, 1997: Parameterization of tropical cirrus ice crystal size distributions and implications for radiative transfer: Results from CEPEX. *J. Atmos. Sci.,* **54,** 2187–2200, doi:10.1175/1520-0469(1997)054<2187:POTCIC>2.0.CO;2.

——, and S. G. Cober, 2004: Single-scattering properties of mixed-phase Arctic clouds at solar wavelengths: Impacts on radiative transfer. *J. Climate,* **17,** 3799–3813, doi:10.1175/1520-0442(2004)017<3799:SPOMAC>2.0.CO;2.

——, J. Um, M. Freer, D. Baumgardner, G. L., Kok, and G. Mace, 2007a: The importance of small ice crystals to cirrus properties: Observations from the Tropical Western Pacific International Cloud Experiment (TWP-ICE). *Geophys. Res. Lett.,* **34,** L13803, doi:10.1029/2007GL029865.

——, G. Zhang, M. R. Poellot, G. L. Kok, R. McCoy, T. Tooman, A. Fridlind, and A. J. Heymsfield, 2007b: Ice properties of single-layer stratocumulus during the Mixed-Phase Arctic Cloud Experiment: 1. Observations. *J. Geophys. Res.,* **112,** D24201, doi:10.1029/2007JD008633.

——, and Coauthors, 2011: Indirect and Semi-Direct Aerosol Campaign: The impact of arctic aerosols on clouds. *Bull. Amer. Meteor. Soc.,* **92,** 183–201, doi:10.1175/2010BAMS2935.1.

Rauber, R. M., and L. O. Grant, 1986: The characteristics and distribution of cloud water over the mountains of Northern Colorado during wintertime storms. Part II: Spatial distribution and microphysical characteristics. *J. Climate Appl. Meteor.,* **25,** 489–504, doi:10.1175/1520-0450(1986)025<0489:TCADOC>2.0.CO;2.

——, and A. Tokay, 1991: An explanation for the existence of supercooled water at the top of cold clouds. *J. Atmos. Sci.,* **48,** 1005–1023, doi:10.1175/1520-0469(1991)048<1005:AEFTEO>2.0.CO;2.

——, and Coauthors, 2014: Stability and charging characteristics of the comma head region of continental winter cyclones. *J. Atmos. Sci.,* **71,** 1559–1582, doi:10.1175/JAS-D-13-0253.1.

Rosenow, A. A., D. M. Plummer, R. M. Rauber, G. M. McFarquhar, B. F. Jewett, and D. Leon, 2014: Vertical velocity and physical structure of generating cells and convection in the comma head region of continental winter cyclones. *J. Atmos. Sci.,* **71,** 1538–1558, doi:10.1175/JAS-D-13-0249.1.

Rutledge, S. A., and P. V. Hobbs, 1983: The mesoscale and microscale structure and organization of clouds and precipitation in midlatitude cyclones. VIII: A model for the "seeder–feeder" process in warm-frontal rainbands. *J. Atmos. Sci.,* **40,** 1185–1206, doi:10.1175/1520-0469(1983)040<1185:TMAMSA>2.0.CO;2.

Schultz, D. M., D. S. Arndt, D. J. Stensrud, and J. W. Hanna, 2004: Snowbands during the cold-air outbreak of 23 January 2003. *Mon. Wea. Rev.,* **132,** 827–842, doi:10.1175/1520-0493(2004)132<0827:SDTCOO>2.0.CO;2.

Sienkiewicz, J. M., J. D. Locatelli, P. V. Hobbs, and B. Geerts, 1989: Organization and structure of clouds and precipitation on the mid-Atlantic coast of the United States. Part II: The mesoscale and microscale structures of some frontal rainbands. *J. Atmos. Sci.,* **46,** 1349–1364, doi:10.1175/1520-0469(1989)046<1349:OASOCA>2.0.CO;2.

Stark, D., B. A. Colle, and S. E. Yuter, 2013: Observed microphysical evolution for two east coast winter storms and the associated snow bands. *Mon. Wea. Rev.,* **141,** 2037–2057, doi:10.1175/MWR-D-12-00276.1.

Syrett, W. J., B. A. Albrecht, and E. E. Clothiaux, 1995: Vertical cloud structure in a midlatitude cyclone from a 94-GHz radar. *Mon. Wea. Rev.,* **123,** 3393–3407, doi:10.1175/1520-0493(1995)123<3393:VCSIAM>2.0.CO;2.

Trapp, R. J., D. M. Schultz, A. V. Ryzhkov, and R. L. Holle, 2001: Multiscale structure and evolution of an Oklahoma winter precipitation event. *Mon. Wea. Rev.,* **129,** 486–501, doi:10.1175/1520-0493(2001)129<0486:MSAEOA>2.0.CO;2.

Wang, Z., and Coauthors, 2012: Single aircraft integration of remote sensing and in situ sampling for the study of cloud microphysics and dynamics. *Bull. Amer. Meteor. Soc.,* **93,** 653–668, doi:10.1175/BAMS-D-11-00044.1.

Westbrook, C. D., and A. J. Illingworth, 2011: Evidence that ice forms primarily in supercooled liquid clouds at temperatures > −27°C. *Geophys. Res. Lett.,* **38,** L14808, doi:10.1029/2011GL048021.

Wexler, R., 1955: Radar analysis of precipitation streamers observed 25 February 1954. *J. Meteor.,* **12,** 391–393, doi:10.1175/1520-0469(1955)012<0391:RAOPSO>2.0.CO;2.

——, and D. Atlas, 1959: Precipitation generating cells. *J. Meteor.,* **16,** 327–332, doi:10.1175/1520-0469(1959)016<0327:PGC>2.0.CO;2.

Wolde, M., and G. Vali, 2002: Cloud structure and crystal growth in nimbostratus. *Atmos. Res.,* **61,** 49–74, doi:10.1016/S0169-8095(01)00102-8.